CZECH TECHNICAL UNIVERSITY IN PRAGUE
FACULTY OF ELECTRICAL ENGINEERING
DEPARTMENT OF RADIOELECTRONICS

SUPPRESSION OF PHOTOBLEACHING IN SUPER-RESOLUTION OPTICAL FLUCTUATION IMAGING USING DIGITAL FILTERING

DIPLOMA THESIS

Author: Bc. Vojtěch Terš

Advisor: Ing. Tomáš Lukeš

ABSTRAKT

Super Resolution Optical Fluctuation Imaging (SOFI) je nová mikroskopická metoda která umožňuje získat obraz ve vysokém rozlišení, jež překonává limit daný difrakcí světla. Photobleaching, který vede k postupné redukci intenzity snímaného signálu v čase, omezuje kvalitu výsledného obrazu, a proto představuje pro SOFI zpracování náročný úkol. Cílem této práce je vyvinout algoritmus pro efektivní korekci photobleachingu pomocí digitální filtrace. Práce předkládá přehled super-resolution metod s důrazem na SOFI a photobleaching. V teoretické části práce jsou dále uvedeny nezbytné základy digitální filtrace. V rámci práce bylo navrženo a implementováno pět nových algoritmů pro korekci photobleachingu a porovnáno se současnými metodami. Jako nejlepší se ukázaly navržené algoritmy založené na filtraci pomocí 1. řádu IIR Butterworth filtru typu horní propust a odečtení střední hodnoty signálu, vypočtené pomocí FIR filtru klouzavého průměru. Rovněž byl vyvinut nový optimalizační algoritmus pro automatický výběr nejvhodnějších parametrů daného filtru. Navržené algoritmy pro potlačení photobleachingu umožňují dosáhnout SOFI obrázků vyšších řádů a zobrazit tak detaily, které jsou s využitím současných metod pro korekci photobleachingu nerozeznatelné.

ABSTRACT

Super Resolution Optical Fluctuation Imaging (SOFI) is a recent microscopy method which allows one to obtain a high-resolution image beyond the diffraction limit of light. Photobleaching, which results in a reduction of the intensity of the acquired signal over time, limits the quality of the final image and therefore represents a challenging tasks for SOFI processing. The goal of this work is to develop an effective algorithm for the correction of photobleaching effect based on digital filtering. Thesis presents an overview of the current super-resolution methods with emphasis on SOFI and photobleaching. Essential basis of digital filtering is also provided in the theoretical part of the work. Five bleaching correction algorithms were developed in this work and compared with the state-of-the-art methods. Proposed algorithms based on the 1st order high-pass IIR Butterworth filter and the moving average subtraction provided the best results superior to the tested state-of-the-art algorithms. An novel optimization algorithm was introduced to automatically select the best filter parameters. The proposed bleaching correction algorithms enable us to achieve higher order SOFI images which contain previously unobservable details.

ACKNOWLEDGEMENT

LIST OF ABBREVATIONS

BW	Bandwidth
CCD	Charge Coupled Device
CMOS	Complementary Metal–Oxide–Semiconductor
DC	Direct Current
FFT	Fast Fourier Transform
FIR	Finite Impulse Response Filter
FWHM	Full With at Half Maximum
GFP	Green Fluorescent Protein
HP	High-Pass
IIR	Infinite Impulse Response
IO	Input-Output
LP	Low-Pass
LTI	Linear Time-Invariant
MSE	Mean Square Error
OTF	Optical Transfer Function
PALM	Photo Activated Localization Microscopy
PSD	Power Spectral Density
PSF	Point Spread Function
SIM	Structured Illumination Microscopy
SMLM	Single Molecule Localization Microscopy
SNR	Signal to Noise Ratio
SOFI	Super resolution Optical Fluctuation Imaging
STED	Stimulated Emission Depletion Microscopy
STORM	Stochastic Optical Reconstruction Microscopy
Zplane	Zero-Pole plot

TABLE OF CONTENTS

1 Introduction

The term super-resolution (SR) microscopy represents methods capable of overcoming the diffraction limit of light. Trying to observe things smaller than about the half of the wavelength of light is challenging due to the diffraction limit specified by Erns Karl Abbe [1]. The maximum resolvable size is defined as $d = \frac{\lambda}{2nsin(\alpha)}$ where n is the refraction index of the observed medium and α is the half-angle of the optical objective lens. The formula $nsin(\alpha)$ can be represented as the Numerical Aperture (NA) which characterizes the lens used. Modern lenses have NA between $1.3 - 1.5$. The resolution of a standard modern microscope is therefore approximately 0.25µm laterally. Although shorter wavelength could be theoretically used, they are impractical for use in cell biology, as they are not compatible with the cell samples.

Because of the diffraction limit, a single light-emitting point observed by a circular optical lens system is visible as an Airy's disc. The visible result of such a point is a 2D impulse response of the system, known as the Point-Spread Function (PSF).
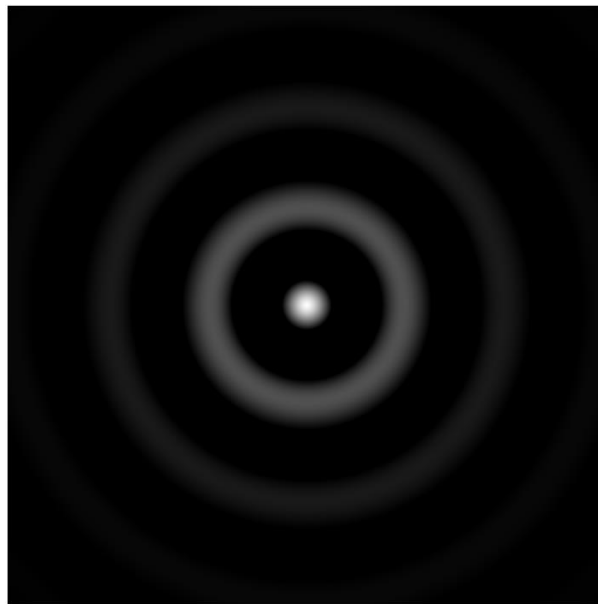
Figure 1 PSF example showing the maximum light intensity (center) along with local minimums and maximums from a single light source. As a result, light emitters are no longer observed as a single points.

As can be seen in Figure 1, the PSF has multiple minimums and maximums, although most of the energy resides in the first maximum. Therefore in commonly used widefield microscopes, the PSFs can be modeled as a single peak 2D Gaussian function [2]. The difference between the ideal and real widefield sample is simulated in Figure 2.

Figure 2 Ideal representation of light emitters (a). Real (Blurry) representation of light emitters due to the convolution with the PSF of the optical system (b).
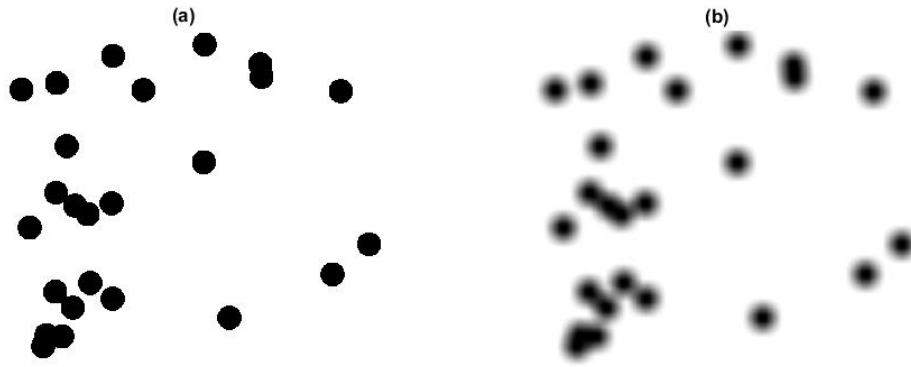
The above mentioned process in Figure 2 can be mathematically described by a 2D convolution. Given an ideal Image F(x,y) (Figure 2 a) and a convolution kernel H(x,y) – PSF in our case, the resulting Image G(x,y) (Figure 2 b) can be obtained as:

$$G(x,y) = \sum_{i=1}^{\infty}\sum_{j=1}^{\infty} F(i,j).H(x-i,y-j) = F*H \tag{1}$$

Where * denotes convolution and [x, y, I, j] are indexes. The Fourier representation of the PSF is a complex Optical Transfer Function (OTF). OTF is further described by the Modulation Transfer Function (MTF) and Phase Transfer Function (PTF). Both of these functions represent the ability of an optical system to transfer spatial frequencies to the image plane at a specific resolution. A good optical system has a wide OTF, so that it can transfer even higher spatial frequencies containing image details [3] [4].

2 Super Resolution Methods

2.1 Structured Illumination Microscopy

In Structured illumination Microscopy (SIM), higher resolution image is reconstructed from multiple samples illuminated using various illumination patterns. By doing so, the higher spatial frequencies (containing image details) are converted into lower-frequencies, where the information can be acquired. The process is shown in Fourier space in Figure 3.
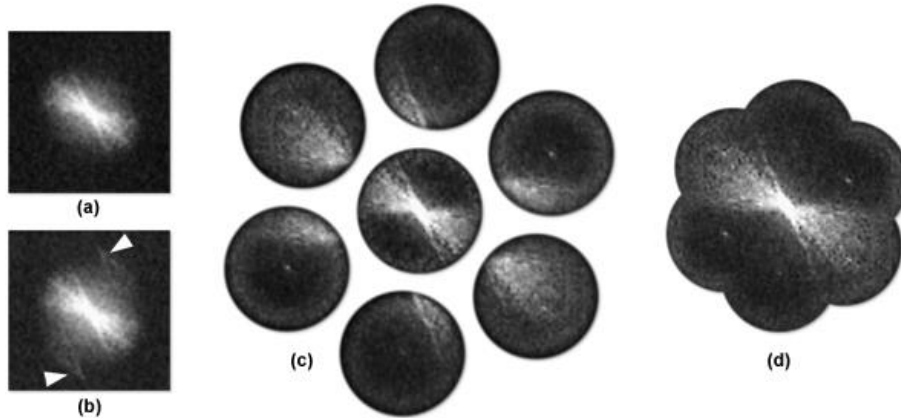

Figure 3 Illustration of the generalized procedure for SIM reconstruction in the Fourier space. (a) Shows the standard Fourier transform of a widefield image with uniform illumination and (b) with structured illumination. The arrows at (b) represents high frequency information that has been copied into lower frequencies. Acquiring three images at different phases of the illumination pattern for each of three rotations of the pattern allows one to compute the spectral components in (c). Shifting each component to its proper position in Fourier space results in an image (d) with approximately twice the frequency radius compared to the conventional image [5].

High resolution image can be reconstructed from multiple low resolution illumination patterned images using various algorithms combining spectral components in Fourier space [6] [7] [8] or using the Bayesian framework [9] [10]. More about SIM algorithms can be found in [11] [12] [13].

2.2 Stimulated Emission Depletion

Stimulated Emission Depletion (STED) is a method requiring a special equipment in the form of 2 precise pulse lasers, which excite and then stimulate fluorescent emission of the examined fluorescent sample. Due to its principle, STED is relatively slow, as it has to scan the sample piece by piece. On the other hand, its resolution is high (~60nm) and generally depends on the emitting intensity of the lasers [1]:

$$d_{sted} = d.\sqrt{1 + \frac{I_{max}}{I_{sat}}} \tag{2}$$

- d   Standard confocal microscope resolution.
- I_{max} Maximum intensity in the center of the reduction beam (second laser).
- I_{sat} Intensity, when the quantum yield is halved due to the stimulated emission [14].

The first laser is responsible for excitation of the sample (Figure 4 left), while the second laser for deactivating surrounding area (Figure 4 center). Due to its complexity and the need for keeping the lasers synchronized, the STED system is generally quite expensive. A simpler method known as Continuous-Wave STED (CW-STED) has been developed [15]. Unlike the classical STED, CW-STED uses

continuous excitation of the sample, but its results have generally slightly worse resolution in comparison with the standard STED.
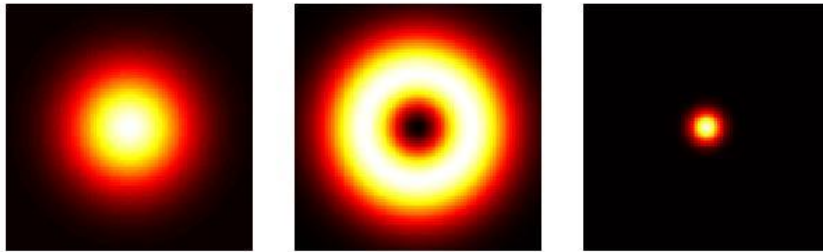
2.3 Single molecule localization microscopy (SMLM)

Stochastic Optical Reconstruction Microscopy (STORM) [17], Photo-Activation Localization Microscopy (PALM) [18] and Fluorescence Photo Activation Localization Microscopy (FPALM) [19] are considered as single molecule localization microscopy (SMLM) methods. They are based on an assumption, that two fluorescent molecules closer than the diffraction limit are not emitting light at once and that their PSF do not overlap. Each of these methods requires the sample to be labeled by a fluorescent dye. Most of the fluorophores are held dark and activated and or deactivated on demand with a laser. The precision of the localization depends on the number of photons N collected from a single emitter and the full width at half maximum (FWHM) of the PSF [19], [20]:

$$d \cong \frac{\Delta_{FWHM}}{\sqrt{N}}$$

(3)

The principle of these methods is shown in Figure 5, where a group of molecules is switched from the off state (dark state) to the on state (bright state) and their positions are recorded. The process is repeated with the next group of molecules until all fluorophores and their positions are successfully captured. The drawback of these methods is that they are time-expensive and not suitable for fast biological dynamics.
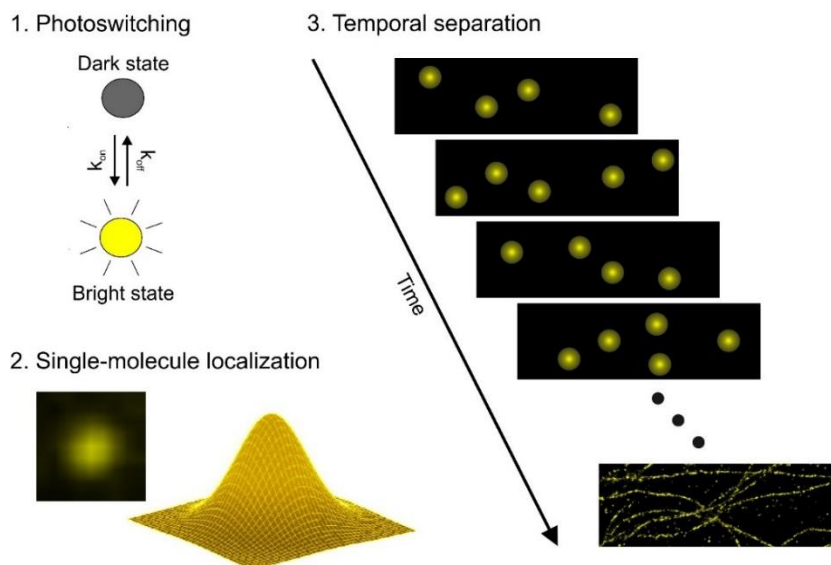

Figure 5 STORM Principle: Molecules are switching between 2 distinguishable (on/off) states (1). Such molecules are localized with a known PSF (2). Nearby molecules are separated in time (3). [21].

3 SOFI

Super resolution Optical Fluctuating Imaging (SOFI) is a super resolution method based on calculation of higher order statistics (namely spatio-temporal cross cumulants) from the input image sequence [22]. A standard CCD/CMOS camera and a widefield microscope can be used to acquire an image sequence of a sample. Both 2D and 3D image series can be acquired, allowing SOFI to improve the resolution in all 3 spatial dimensions [22], [23]. In this work however, I will focus on 2D SOFI processing only. A simplified 2D image sequence is shown in Figure 6. The acquired image is in fact a 3D image stack with the 3rd dimension being the time.
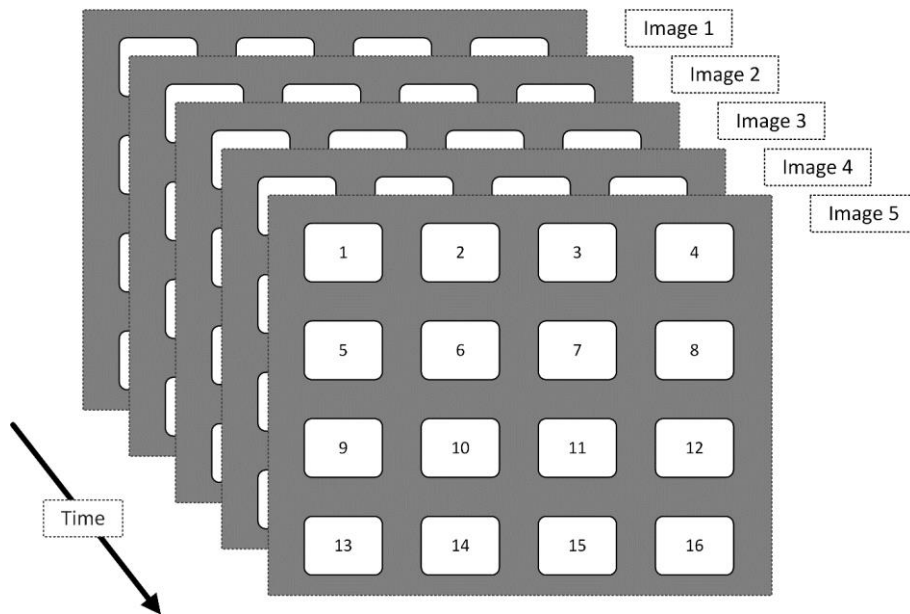

Figure 6 SOFI Image capture demonstration showing the time series of simple 2D images

SOFI is using fluorescently labeled samples where the fluorophores have to exhibit at least 2 optically distinguishable states (on-off) [22] . The sample is excited by a source of light and then captured by camera. Because it takes some time for the fluorophores to blink randomly after excitation, it is almost always necessary to remove some frames at the beginning captured just after excitation. The present process of calculating a high-resolution SOFI image may include photobleaching correction and molecule drift correction. After these corrections, SOFI image is constructed (Section 3.1). Finally a deconvolution can be applied to further enhance the image.

3.1 SOFI principle

Let us assume a sample composed of N independently fluctuating emitters located at positions r_k and having a time-dependent molecular brightness $\varepsilon_k s_k(t)$, where ε_k is the constant molecular brightness and $s_k(t)$ is the time-dependent fluctuation.

$$\sum_{k=1}^{N} \delta(\boldsymbol{r} - \boldsymbol{r_k}) \varepsilon_k s_k(t) \tag{4}$$

We further assume, that the position of emitters doesn't change over time. Molecule drifts can be corrected before calculating SOFI Image. Additional assumption includes that the PSF doesn't vary locally although even this can be taken into account. The Fluorescent signal at position **r** and time t F(**r**,t) is the result of convolution of all the emitters with the system's PSF U(**r**) [22]:

$$F(\boldsymbol{r}, t) = \sum_{k=1}^{N} U(\boldsymbol{r} - \boldsymbol{r_k}) . \varepsilon_k s_k(t) \tag{5}$$

The fluctuations can be further expressed as zero-mean fluctuations [22]:

$$\begin{aligned} \delta F(\boldsymbol{r}, t) &= F(\boldsymbol{r}, t) - \langle F(\boldsymbol{r}, t) \rangle_t \\ &= \sum_k U(\boldsymbol{r} - \boldsymbol{r_k}) . \varepsilon_k \left[s_k(t) - \langle s_k(t) \rangle_t \right] \\ &= \sum_k U(\boldsymbol{r} - \boldsymbol{r_k}) . \varepsilon_k \, \delta s_k(t) \end{aligned} \tag{6}$$

The second order autocorrelation function G$_2$(**r**,t)is then given by [22]:

$$\begin{aligned} G_2(R, t) &= \langle \delta F(\boldsymbol{r}, t + \tau) \delta F(\boldsymbol{r}, t) \rangle_t \\ &= \sum_{j,k} U(\boldsymbol{r} - \boldsymbol{r_j}) . U(\boldsymbol{r} - \boldsymbol{r_k}) . \varepsilon_j . \varepsilon_k \langle \delta s_j(t + \tau) \delta s_k(t) \rangle \\ &= \sum_{j,k} U^2(\boldsymbol{r} - \boldsymbol{r_j}) . \varepsilon_k{}^2 \langle \delta s_k(t + \tau) \delta s_k(t) \rangle \end{aligned} \tag{7}$$

In Eq. (7), we have assumed, that the emission of different emitters is not correlated in time, so that all cross terms $\langle \delta s_j(t + \tau) \delta s_k(t) \rangle$ with $j \neq k$ vanish [22]. The second order autocorrelation function becomes a sum of squared PSF weighted by molecular brightness ε_k and molecular correlation function $\langle \delta s_k(t + \tau) \delta s_k(t) \rangle$. We further assume the PSF to be 2D Gaussian function defined as [24] :

$$f(x, y) = A . e^{\left(\frac{(x-x_0)^2}{2\sigma_x^2} + \frac{(y-y_0)^2}{2\sigma_y^2} \right)} \tag{8}$$

Taking Eq. (8) to the second power yields a resolution improvement by a factor of $\sqrt{2}$ as shown in Figure 7 for a 1D case. The 2nd order autocorrelation function resulted in $\sqrt{2}$ resolution improvement. Higher orders can be used to further increase the resolution of a SOFI image, they are however no longer considered correlations, but rather cumulants. Unlike higher order correlations, higher order cumulants contain only the Nth power of the PSF and no lower order cross terms which would hamper the resolution enhancement. Additional information about the cumulant calculation can be found for example in [22].
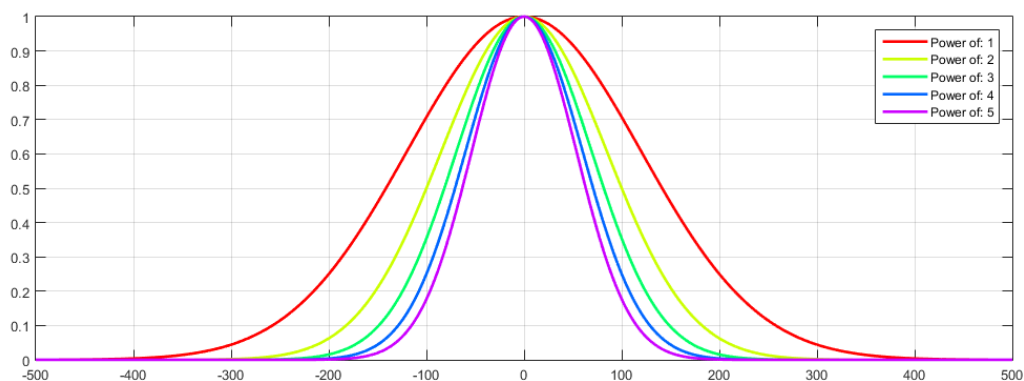
Figure 7 Normalized 1D Gaussian function raised to the Nth power. With increasing power (i.e. order of the SOFI analysis) the PSF shrinks by a factor of $\sqrt{N}$. It can be seen that 4th order leads to 2 times resolution improvement compared to the first order.

3.2 Fluorescence and photobleaching

Fluorescence represents the emission of photons by atoms or molecules that were previously excited by external radiation into higher emission states. In Niels Bohr's atom model, electrons are located only in specific orbits around the center. The higher the distance from the center, the more energy they have. Under specific circumstances (external excitation), they can eventually reach orbits with higher energy states. Once they reach the excitation state, several process can occur which among them, fluorescence is the most important. The diagram showing these process is depicted in Jablonski Diagram in Figure 8.
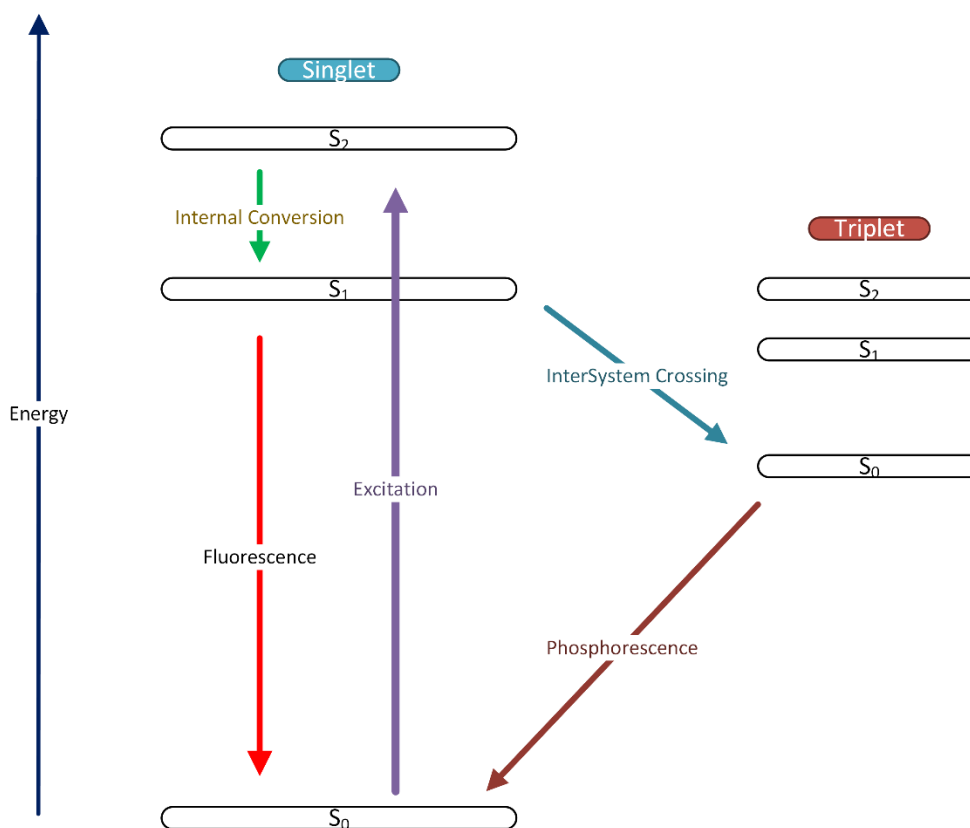

Figure 8 Simplified Jablonski diagram showing the processes that may occur after excitation of a molecule. The model consist of 3 energy states and several processes: Violet – External Excitation, Green – Internal Conversion, Red – Fluorescence, Light Blue – Intersystem Crossing from singlet state into the Triplet State and the dark red – Phosphorescence.

Photobleaching is an irreversible process in which a fluorescent dye or a fluorophore molecule loses the fluorescence due to photochemical reactions and or cleaving of covalent bonds. [25, p. 228]. The cleavage happens when the molecule enters the triplet state from excited singlet state, during which it can interact with nearby molecules and cleave the covalent bonds. Because the triplet state is long-lived in respect to the singlet state, the cleaving has much more time to interact with the nearby molecules [25, p. 229]. The average number of excitation and emission states depends on the used dye and molecular structure of the sample [25, p. 229]. However it always leads to a situation, where a camera with a given quantum efficiency is able to absorb decreasing number of photons, leading to darker and darker images as the time goes by. This is a serious problem in time-lapse microscopy such as SOFI. The effect of photobleaching is clearly visible in Figure 9 taken from [26].
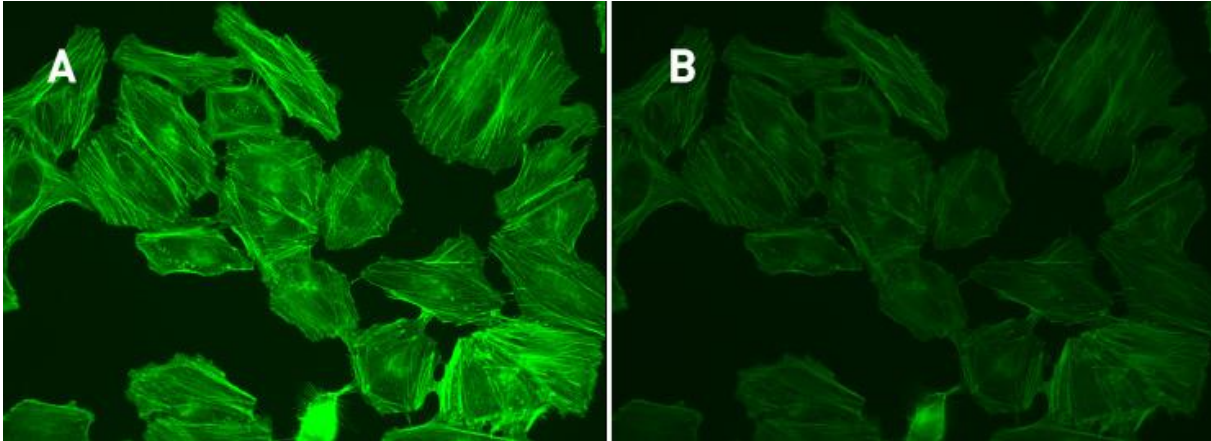

Figure 9 Hela cells -   (A) shows the initial intensity of the fluorophore, while panel (B) shows the photobleaching that occurs after 36 seconds of constant illumination [26].

3.3 Bleaching correction

There are currently 2 methods that can be applied to suppress the photobleaching effect in SOFI:

- Division into subsequences
- Inverse exponential fitting

For SOFI, an image sequence is required which usually consists of thousands of images acquired over time. If we assume the photobleaching effect to be neglectable over a "short" time span, the raw image sequence can be split into sub sequences (of usually hundreds of images) which are processed separately. The resulting SOFI images from all the sub sequences are then averaged to obtain the final SOFI image. This method however limits the attainable resolution improvement, because higher cumulant orders do need longer sequences, so that they have enough blinking events of the emitters for the high-resolution image reconstruction.

The inverse fitting method assumes the photobleaching effect to have an exponential character i.e. the intensity of the emitters exponentially decreases in time as shown in Figure 10 where the mean trace of a simulated 2D Stack of 3000 images is computed along with the exponential fit curve in form of Eq. (9) where coefficients a, b and c are calculated based on the Least Mean Square Error (MSE).

$$a.e^{(\frac{-x}{b})} + c \tag{9}$$

Eq. (9) can be slightly changed to bi-exponential formula as stated for example in [27]. The overall inverse fitting algorithms however always assume the photobleaching effect to have the exponential character. During this procedure, all pixels are treated the same way, causing black noisy pixels to increase the signal intensity and decrease the overall quality of the image. The exponential curve can

be alternatively created pixel-wise, but this method is extremely computationally demanding. Moreover its results are not completely satisfying. Comparison with the moving average subtraction technique (later explained in Section 6.2) can be found in Appendix A, Figure 54 and Figure 57.
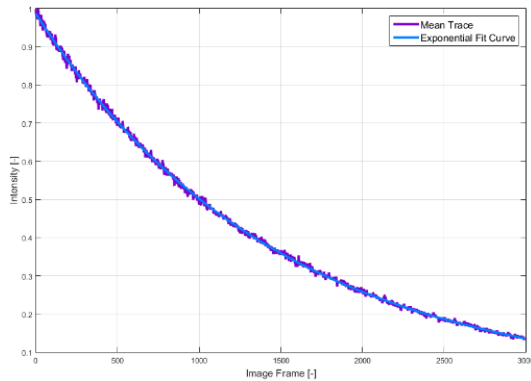

Figure 10 Mean trace of simulated data set showing the photobleaching effect and its exponential fit curve.
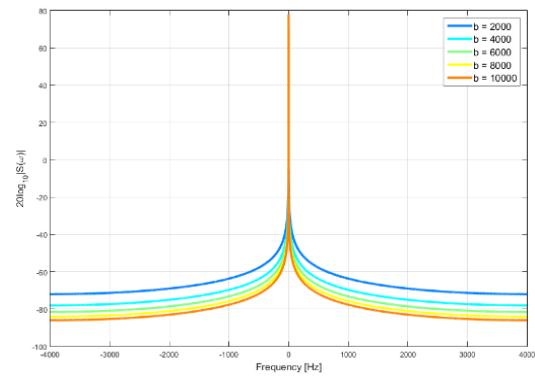

Figure 11 Influence of b - coefficient from Eq. (9) on the signal's PSD. Model with sampling frequency f_s = 8000 Hz.

Assuming the exponential characteristics of the photobleaching, we can investigate the spectrum of such a signal using the Fourier transform. First of all, the c – coefficient represents just a DC offset and can be ignored as it does not have any real impact on the signal itself. We can now take a look at the two other remaining coefficients a, b (assuming both are positive):

$$\int_0^\infty ae^{-\frac{t}{b}} \cdot e^{-i2\pi ft}dt = \frac{ba}{2i\pi bf + 1} \tag{10}$$

The a – coefficient act as a "spectrum multiplier ". The lower the coefficient is, the lower Power Spectral Density (PSD) of the signal we can expect. The b – coefficient, sometimes referenced as the exponential decay, is a bit more problematic. If we take the limit of $f \to \infty$ in Eq. (10), the PSD at the infinite frequency goes to zero, however because the real SOFI images tend to have sampling frequency around 100 Hz and because the b – coefficient varies in practice in the order of thousands, we cannot ignore it completely. The chart in Figure 11 shows the influence of various b-coefficients on the PSD.

With increasing b, the PSD of the signal decreases and most of the signal power tends to be located at the DC (the zero frequency). There are 2 main results from this investigation:

- Photobleaching can be filtered in frequency domain using custom high-pass filters.
- Photobleaching cannot be removed completely due to the exponential shape of its PSD.

4 Filters

In this chapter, we will take a look at the most common analog and digital filters with different properties, approximations and design strategies. Filters are used in signal processing for suppression of unwanted frequencies and can be found almost in every electronic component in various forms. From the frequency point-of-view, they can be divided into the following categories (Figure 12):

- Low-pass (LP) filters
- High-pass (HP) filters
- Band-pass filters

- Band-stop filters
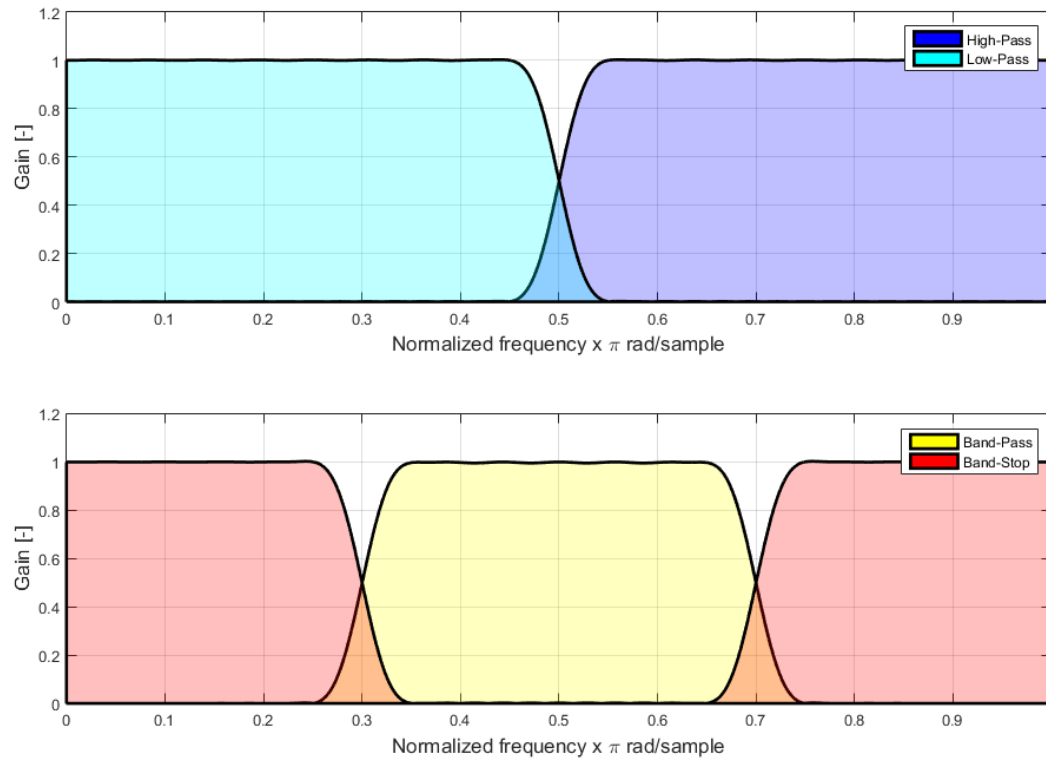- Multi-band (pass/stop) filters

Figure 12 Basic filter types from frequency-domain point of view. Low-pass and high-pass filters (top) with normalized cut-off frequency of 0.5 π rad/sample. Band-pass and band-stop filters (bottom) with normalized cut-off frequencies of 0.3 and 0.7 π rad/sample.

Each filter has at least 1 passband, 1 stopband and 1 transition band. Signal composed of multiple frequencies in the passband range of the filter passes through unattenuated while frequencies in the stopband of the filter are not allowed to pass. Ideally, there would be no such frequencies in the filter's output, however real filters always just attenuate the unwanted signal. The attenuation is not infinite and depends on the filter's design. The last part of each filter's frequency prototype is the transition band. This is a band that must be sacrificed for real filter design. This will be explained later, but for now it is sufficient that the transition band should be usually as narrow as possible.

Each filter can be described by a general operator H and an input-output (IO) formula [28]:

$$y = H[x]$$

(11)

Figure 13 General discrete system with x and y representing the input and output signals. H is a general operator.

In Figure 13, y is the output of the system, H is the system's operator and x is the system's input. Further in this work, we will assume 2 important properties of these systems.

- **LINEARITY**
- **TIME—INVARIANCE**

Linearity can be understood so that the principle of superposition can be applied to obtain the output signal. The time-invariant property means that the system's response doesn't change with time, e.g. we obtain the same result in time t_1 as in time t_2 where $t_1 \neq t_2$. If the system is both linear and time-invariant, we say it's an **LTI** system.

4.1 Impulse response

Impulse response is the output of any arbitrary previously relaxed LTI system excited by a unitary pulse. The impulse response $h(t)$ is one of the main filter charasteristics. Its knowledge is crucial in determining the system's stability and causality, which will be described later in Section 4.3 and 4.4. Given the knowledge of $h(t)$, we can construct the IO relationship as follows [29]:

Continuous time: $\qquad y(t) = \int_{-\infty}^{\infty} x(\tau)\, h(t-\tau)\, d\tau$

Discrete time: $\qquad y[k] = \sum_{i=-\infty}^{\infty} x[k]h[k-i]$ $\hfill$ (12)

The integral in Eq. (12) is also known as the convolution integral and the expression can be written as:

$$y(t) = x(t) * h(t) \tag{13}$$

Impulse response defines what delay is needed for the filter to work as intended. This delay is generally defined as the length of the impulse response due to the convolution formula in Eq. (13), which in case of Finite Impulse Response (FIR) filters corresponds to the number of delay blocks they have.

4.2 Transfer function

Transfer function of the system (i.e. the frequency response) is defined as the Fourier transform of the filter's impulse response.

$$H(\omega) = \int_{-\infty}^{\infty} h(t)e^{-j\omega t}\, dt \tag{14}$$

If we further apply the convolution property of the Fourier transform onto Eq. (13) we get:

$$Y = H.X \tag{15}$$

In Eq.(15) H and X are the Fourier transformed impulse response and the signal, respectively. This is a commonly used formula for system description in frequency domain. In fact most signal processing tasks can be processed in the frequency domain (including digital filtering) taking into account the Fast Fourier Transform (FFT) that is just a fast numerical method for solving the Discrete Fourier Transform (DFT). Because of the discrete implementation of convolution, Eq. (15), must be processed in Fourier space with additional zero-padding to avoid border problems.

4.3 Stability

A system is stable, if the improper integral from its impulse response $h(t)$ converge to a finite number:

Continuous time [30]: $\qquad \int_{-\infty}^{\infty} |h(t)|\, dt < \infty$

Discrete time $\quad$ [30]: $\qquad \sum_{-\infty}^{\infty} |h[k]| < \infty$ $\hfill$ (16)

As a consequence, any Finite Impulse Response (FIR) filter is stable and stability condition has to be evaluated only in case of Infinite Impulse Response filters (IIR). An integrator circuit shown in Figure 14 is a classic example of an unstable system.
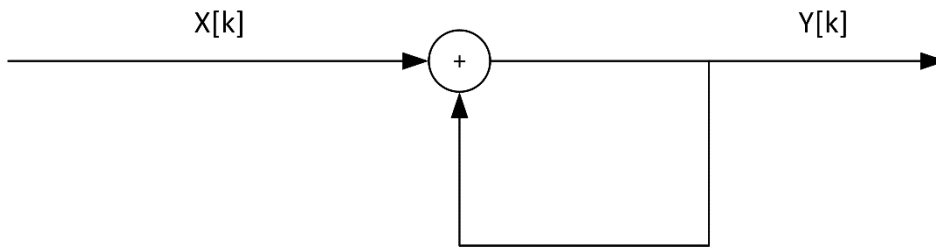

Figure 14 Discrete Integrator with a difference equation of Y[k] = Y[k] + X[k] is a standard example of an unstable system.

4.4 Causality

The system is causal if its impulse response starts at time $t_2 \geq t_1$. Where t_1 is the time, when the system is beeing excited by an impulse. In other words, the system cannot produce anything until the excitation signal reaches its input. Examples of causal and non-causal impulse responses are shown in Figure 15.
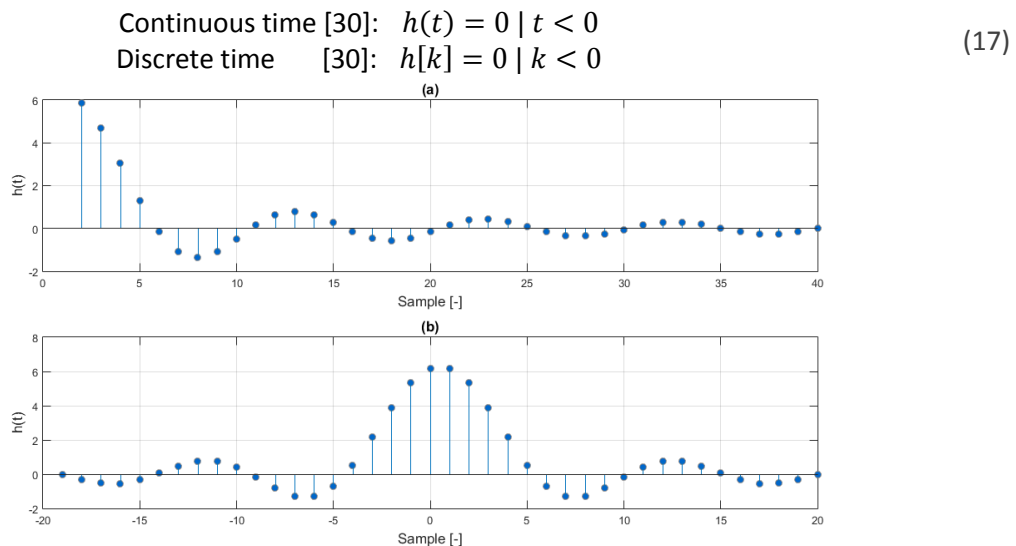
$$\text{Continuous time [30]:} \quad h(t) = 0 \mid t < 0$$
$$\text{Discrete time} \quad \text{[30]:} \quad h[k] = 0 \mid k < 0 \tag{17}$$

Figure 15 Example of a causal impulse response (a) and non-causal impulse response (b) – cannot be realized.

We can now determine why ideal filters cannot be constructed. The ideal filter's transfer function $H(\omega)$ is in the shape of a rectangle with a single passband and a single stopband without any transition bands. The required impulse response fur such an ideal filter is according to Eq. (14) the inverse Fourier Transform of the frequency response. By using Fourier Transform identities from [31], we can obtain the formula for such an impulse response: $h(t) = \dfrac{\sin(t)}{t}$

We can see, that the function runs toward infinity on both sides, this would require the filter to have infinite impulse response at first (which is still possible), but also to take into account all samples from the past (t < 0), including samples from $-\infty$. This is of course impossible and such a system cannot be constructed. We say that such a system is non-causal.

4.5 Digital filters

This chapter describes the design, types and properties of digital filters. Although analog filters will be used across this chapter as well, their intention is to show standard design procedures.

Using a Z transform, a digital filter can be described by a discrete polynomial representation of a transfer function. More about the Z-Transform can be found in [28] [32] [29] [31].

$$H[z] = \frac{Y[z]}{X[z]} = \frac{b_0 + b_1 z^{-1} + \cdots + b_n z^{-n}}{a_0 + a_1 z^{-1} + \cdots + a_n z^{-n}} \qquad (18)$$

The discrete transfer function can be further factorized to obtain [28, p. 156]:

$$H[z] = \frac{b_0(z - q_1)(z - q_2) \dots (z - q_n)}{(z - p_1)(z - p_2) \dots (z - p_n)} \qquad (19)$$

Where $q_1, q_2 \dots q_n$ are the Zeros and $p_1, p_2 \dots p_n$ are the Poles of a filter's transfer function. Finite impulse response filters (FIR) have only zeros and are therefore represented by the b-coefficients. On the other hand, infinite impulse response filters may contain both zeros and poles. The filter's stability can be evaluated using a zero-pole plot (Z plane), which is a complex plane with position of all the filter's zeros and poles.

4.5.1 Finite impulse response filters

Finite Impulse Response filters are always causal and stable. Their order corresponds to the number of delay blocks. They are easy to implement and design and their structure always copy the structure shown in Figure 16. I will further describe the standard procedure of designing a high-pass FIR filter known as windowing.
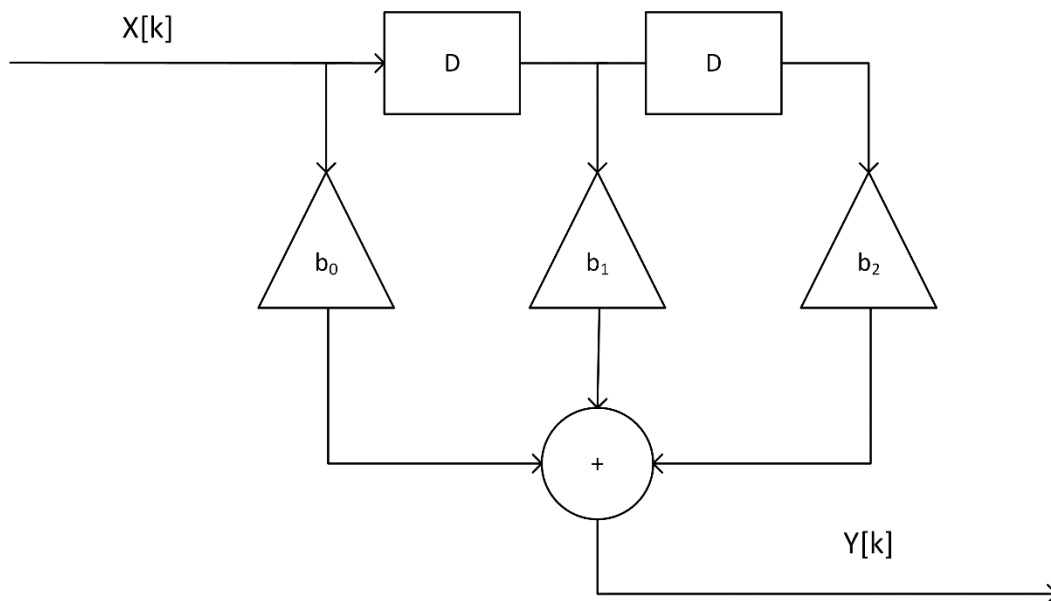

Figure 16 Simple FIR Filter structure with 2 delay blocks and 3 coefficients. Higher orders are created by adding additional delay blocks and multiplier sections. The design of such a filter always end up by choosing the correct coefficients, which are in most cases related to window functions used for the filter design.

Blackman-Harris window [33]

$$W(n) = a_0 - a_1 \cos\left(\frac{2\pi}{N-1}\right) + a_2 \cos\left(\frac{4\pi}{N-1}\right) - a_3 \cos\left(\frac{6\pi}{N-1}\right)$$
$$a_0 = 0.35875 \mid a_1 = 0.48829 \mid a_2 = 0.14128 \mid a_3 = 0.01168$$

(20)

Blackman window [34]

$$W(n) = 0.42 - 0.5 \cos\left(\frac{2\pi n}{N-1}\right) + 0.08 \cos(\frac{4\pi n}{N-1})$$

(21)

Hamming window [35]

$$W(n) = 0.54 - 0.46 \cos(\frac{2\pi n}{N})$$

(22)

Nuttall window [36]

$$W(n) = a_0 - a_1 \cos\left(\frac{2\pi}{N-1}\right) + a_2 \cos\left(\frac{4\pi}{N-1}\right) - a_3 \cos\left(\frac{6\pi}{N-1}\right)$$
$$a_0 = 0.363582 \mid a_1 = 0.489177 \mid a_2 = 0.136599 \mid a_3 = 0.010641$$

(23)

Hann window [37]

$$W(n) = 0.5\left(1 - \cos(\frac{2\pi n}{N})\right)$$

(24)

Kaiser window [38]

$$W(n) = \frac{I_0\left(\pi\alpha\sqrt{1 - \left(\frac{2n}{N-1} - 1\right)^2}\right)}{I_0(\pi\alpha)}$$

I_0 … 0th Bessel function of the first kind α … Modifies window shape

(25)

Gauss window [39]

$$W(n) = e^{-\frac{1}{2}\left(\alpha\frac{n}{(N-1)/2}\right)^2}$$

(26)

Flat-top window [40]

$$W(n) = a_0 - a_1 \cos\left(\frac{2\pi n}{N-1}\right) + a_2 \cos\left(\frac{4\pi n}{N-1}\right)$$
$$-a_3 \cos\left(\frac{6\pi n}{N-1}\right) + a_4 \cos\left(\frac{8\pi n}{N-1}\right)$$
$$a_0 = 0.215579 \mid a_1 = 0.416632 \mid a_2 = 0.2772632$$
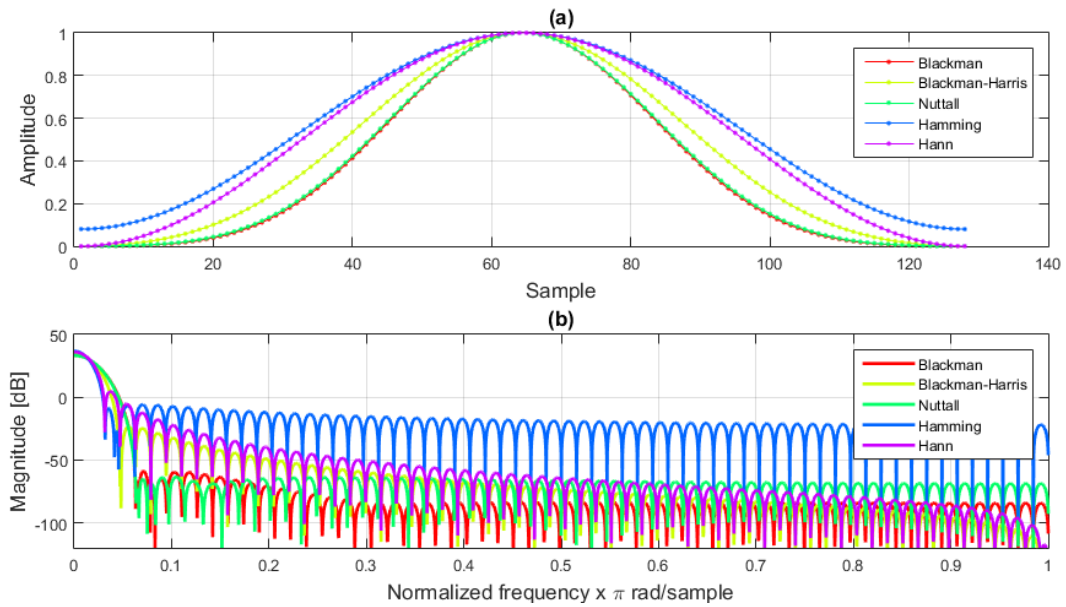$$\mid a_3 = 0.083579 \mid a_4 = 0.0069474$$

(27)

Figure 17 Selected windows both in time domain (a) and Fourier space (b).

The design of an arbitrary FIR filter using the windowing technique follows the design of an ideal low-pass filter with rectangular transfer function. As was mentioned earlier in Section 4.4 , such a filter has an impulse response with a shape of a sample function, which cannot be realized. Therefore the first and necessary operation is to cut the impulse response on both sides to make it finite. Furthermore, because such a result is still not causal, it needs to be shifted on the time axis so that it starts at t = 0. Additionally, because the trim of the impulse response included a rectangular multiply, which is not suitable for filter design due to its low 1st side lobe attenuation in the stopband of only 13 dB (see Figure 19, where the rectangular window function is compared against other window functions), additional weighting of the impulse response is usually required. This involves the multiply of an ideal impulse response with a custom window function with better Fourier properties. The design is therefore in most cases dependent on the window function used for final weighting of the impulse response. These steps are illustrated in Figure 18, where the Hamming window function was used.

The definition of a discrete-time sample function follows [29]:

$$h[k] = \frac{\sin(\omega_c[n-M])}{\pi(n-M)} \mid h[k] = 2ft \;\; k \in \langle\frac{M}{2}\rangle$$
$$N = Number\ of\ window\ samples \left| M = \frac{N-1}{2} \right| ft = \frac{fc}{fs}$$

(28)

Note that a FIR 30th order filter needs 31 window samples. The ω_c in Eq. (28) is a normalized frequency in range $\omega_c \in (0,1)$ π rad/sample. The filter order can be increased by increasing the number of samples taken from the sample function. The impact of increasing the filter order is shown in Figure 20. It is clear that the stopband is attenuated at -60dB with relatively low transition band.
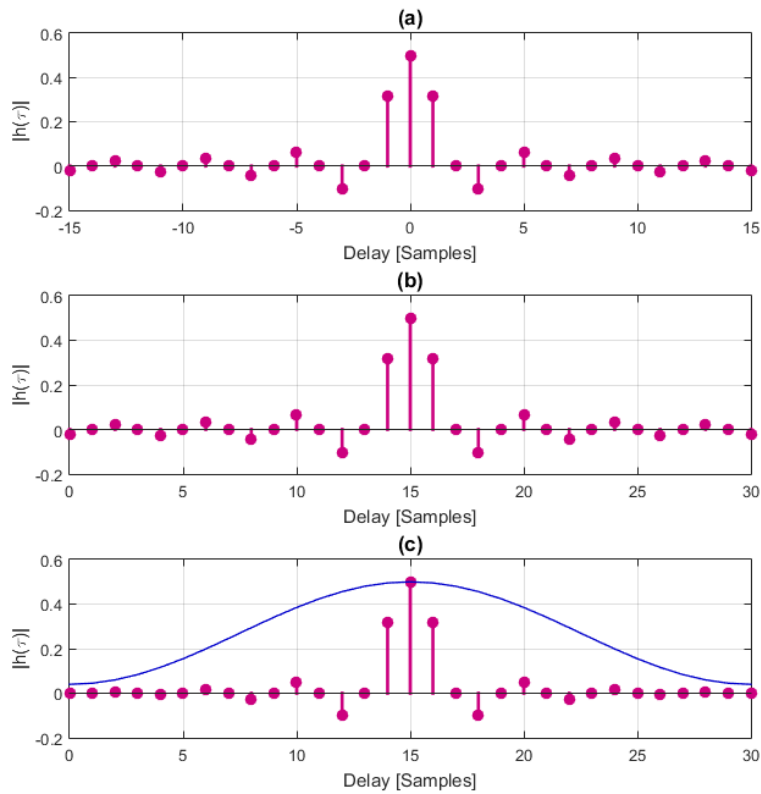
Figure 18 Process of transforming an ideal filter's impulse response (a) into a feasible time-shifted impulse response (b) further weighted by a custom window function (Hamming) to create filter with better performance (c).
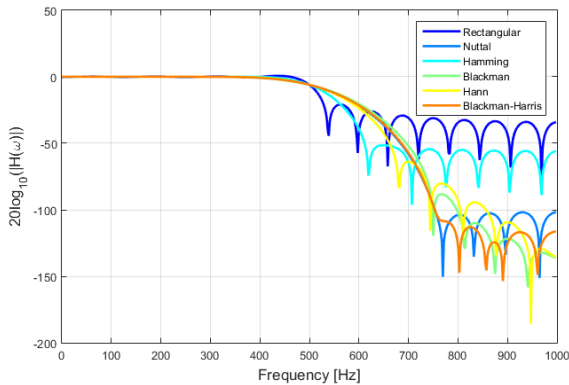

Figure 19 Low-pass 31th order FIR filter with f_c = 500 Hz and f_s = 2K Hz designed by different window functions. The window function affects the final attenuation of the filter in the stopband as well as the width of the transition band.
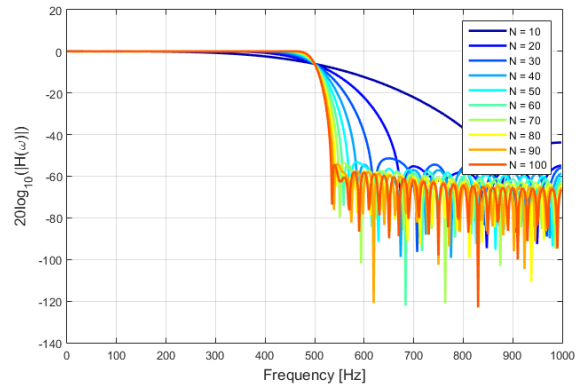
Figure 20 Low-pass FIR filter with f_c = 500 Hz and f_s = 2 KHz. Filter's impulse response is customized by Hamming window. Increasing the filter order (N) results in a narrow transition band, which is mostly a required attribute.

To design other filter types (high-pass, band-pass, band-stop), one would also have to start with a low-pass design and then transform it into the selected filter type. Because the primary goal of this chapter was not to design a low-pass, but rather a high-pass filter for bleaching correction, the next step is to transform the low-pass into the high-pass. This can be done by combining an all-pass filter ($|H(\omega)|$ = const = 1) with our designed low-pass filter. The high-pass is then the low-pass subtracted from the all-pass and its impulse response is therefore inverted [41]:

$$h[k] = \frac{-\sin(\omega_c[n-M])}{\pi(n-M)} \mid h[k] = 1 - 2ft \ \ k \in \langle \frac{M}{2} \rangle \tag{29}$$

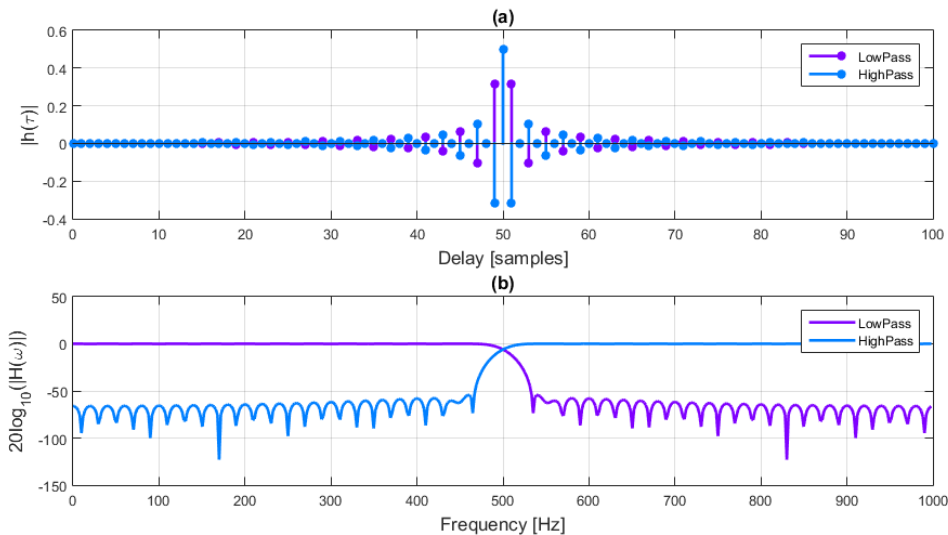Example and comparison of the frequency and impulse responses are shown in Figure 21.

Figure 21 Hamming 100th order digital FIR low-pass & high-pass designs with cut-off frequency f_c = 500 Hz and sampling frequency f_s = 2 KHz. The inversion of both the Impulse response (a) and the frequency characteristics (b) is clearly visible.

4.5.2 Infinite impulse response filters

As we have seen in the previous examples, FIR filters do have some very important properties:

- Easy to design and implement (Consisting only of choosing the desired filter order and the right window function).
- Always stable with a finite impulse response (They do not have any feedback and only finite number of delay loops that specify the filter's order).

The advantage of IIR filters over FIR filters lies in the fact that IIRs use both zeros and poles in filter design, allowing them to have steeper transition between the pass and the stop bands. IIR filters need lower orders to satisfy the design requirements. This feature is advantageous in situations where a limited filter order must be implemented. (See Figure 22 for comparison).
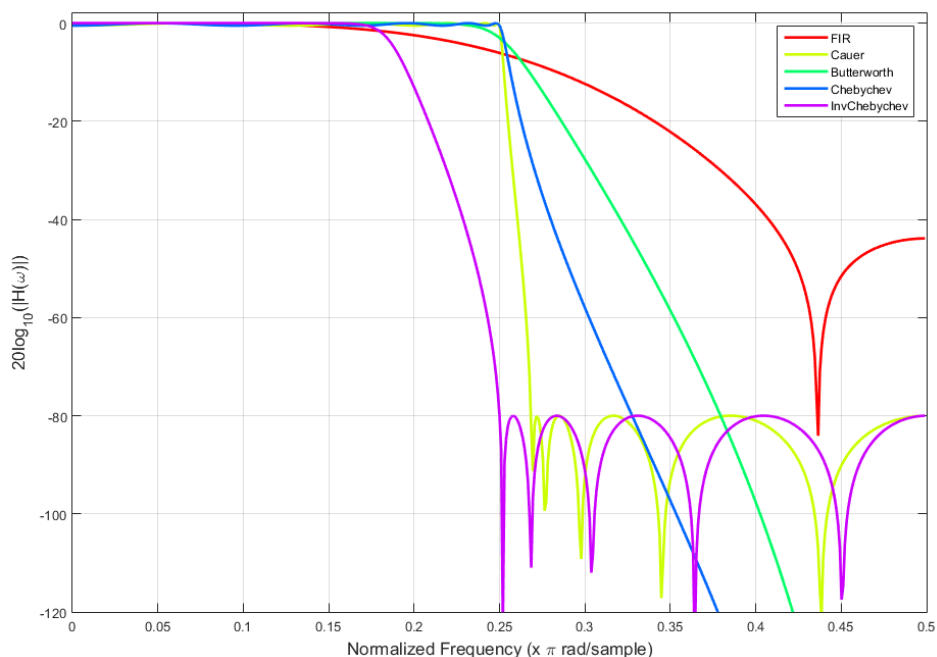

Figure 22 Single FIR and multiple IIR filter approximations comparison with a constant filter order showing that FIR filters need higher orders to satisfy the design parameters. The cut-off frequency of 0.25 π rad/sample is equal for all filter types.

~ 17 ~

4.5.2.1 Butterworth IIR approximation

Butterworth is a special IIR filter with maximally flat characteristics in the passband. Its Nth order low-pass transfer function is defined as [28, pp. 65-76]:

$$H(s) = \frac{1}{\prod_{i=i}^{N}(s - s_i)} \tag{30}$$

We can see, that the transfer function will always have N poles and no zeros. S_i are the complex roots:

$$S_i = -\sin\left(\pi \frac{2i-1}{2N}\right) + icos(\pi \frac{2i-1}{2N}) \tag{31}$$

The design starts as in the case of FIR filters with a normalized low-pass filter design followed by custom frequency transforms and finally by conversion into digital domain. A prototype of such a filter is shown in Figure 23 (a) along with its complex roots locations Figure 23 (b). The normalized low-pass filter can be transformed into a different cut-off frequency low-pass filter or into the high-pass filter [32, pp. 81-82]. An example is given in Figure 24 with a custom cut-off frequency f_c = 6000 Hz.

- Low-pass to low-pass: $s = \frac{f_0}{f_c}f$
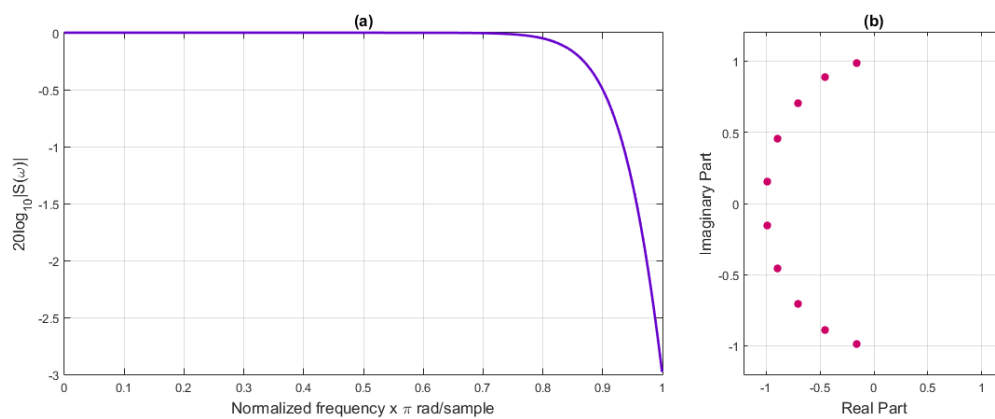- Low-pass to high-pass: $s = \frac{f_0 f_c}{f}$

Figure 23 Normalized 10th order low-pass Butterworth filter transfer function (a) with its complex roots (b).
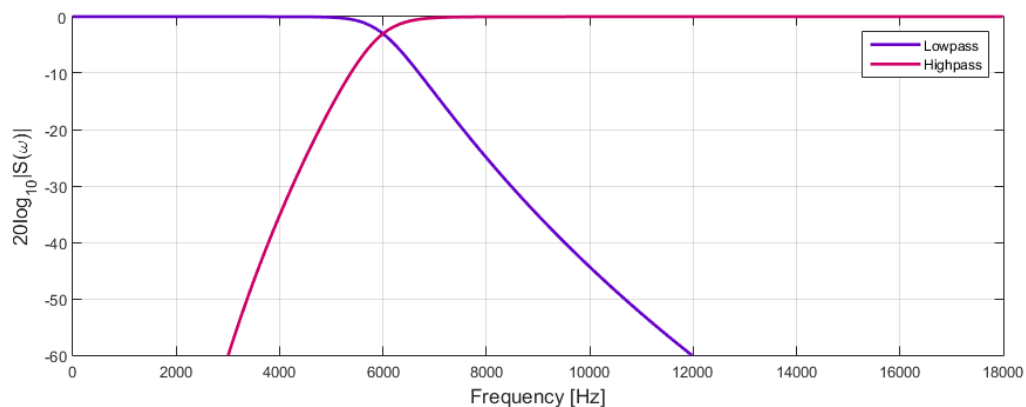

Figure 24 Butterworth 10th order IIR filter with cut-off frequency of 6000 Hz. Both low-pass and high-pass versions.

Additional band-pass and band-stop transforms can be found also in [32]. Bilinear transform for conversion from analog domain into the digital domain will not be discussed here. Additional information can be found for example in [32, p. 86] or Appendix A, Figure 55.

4.5.2.2 Chebyshev IIR approximation

Chebyshev filters overall decrease the transition band by allowing the transfer function to ripple in the passband (Chebyshev) or in the stopband (inverse Chebyshev). The general formula for the Chebyshev transfer function follows [28, p. 77]:

$$|H(i\omega)|^2 = \frac{1}{1 + \epsilon^2 T_N^2(\omega)} \tag{32}$$

Where $\epsilon^2 = 10^{\frac{r}{10}} - 1$, r is the passband ripple in dB and $T_N(\omega)$ is the Nth Chebyshev polynomial. According to [32, p. 71] the polynomial can be easily generated using recursion formula:

$$T_0(x) = 1 \mid T_1(x) = x$$
$$T_{n+1}(x) = 2xT_n(x) - T_{n-1}(x) \tag{33}$$

As can be seen from an example of 7th order Chebyshev digital low-pass filter with allowed passband ripple ϵ = 10dB in Appendix A, Figure 52, the designed filter's transfer function has a 10dB ripple in the passband and no ripple in the stopband. The filter is stable according to its impulse response and its Z-plane shows multiple zeros (point) and poles(cross) lying in the complex ring with absolute value less than 1, which is also a criterion for the filter's stability. If the allowed passband ripple is decreased to a minimum, the Chebyshev filter becomes the Butterworth filter instead [42, p. 333].

4.5.2.3 Inverse Chebyshev IIR approximation

The only difference when comparing the inverse Chebyshev filter with the standard Chebyshev filter is that its transfer function has a ripple ϵ defined in the stopband. The transfer function formula for the inverse Chebyshev filter is [32, p. 72] :

$$|H(i\omega)|^2 = \frac{\epsilon^2 T_N^2(\omega)}{1 + \epsilon^2 T_N^2(\omega)} \tag{34}$$

Where ϵ is the allowed ripple in the stopband (i.e. the minimal attenuation in the stopband). Chebyshev polynomials can be calculated the same way as in the case of Chebyshev filter design (Section 4.5.2.2, Eq. (33)). A 7th order low-pass digital inverse Chebyshev filter with stopband ripple ϵ = 40dB is in Appendix A, Figure 53 along with its impulse response and the Z plane.

4.5.2.4 Cauer (Elliptical) IIR approximation

Cauer filter or Elliptical filter combines properties from both Chebyshev designs, allowing ripple both in the passband and the stopband. It has the sharpest transition between bands compared to the previous IIR filters. The general formula for the transfer function is given by [32, p. 73]:

$$|H(i\omega)|^2 = \frac{1}{1 + \epsilon^2 U_N^2(\omega, L)} \tag{35}$$

Where ϵ is the allowed passband ripple and $U_N(\omega, L)$ is the Jacobian Elliptic function of Nth order with respect to parameter L containing the information about the relative heights of the ripples. Further information about Cauer filter design can be found in [28, pp. 93-108] . A 7th order Cauer filter example is given in Appendix A, Figure 56 showing the transfer function, impulse response and the Z plane.

5 Methods

I tested the proposed bleaching correction algorithms using 2 test samples of living Hela cells. Figure 25 shows widefield image (average of the image stack over time) of the vimentin of living Hela cells labeled with Dreiklang fluorescent protein. The test samples were prepared and kindly provided by Mr. Azat Sharipov and Dr. Stefan Geissbuehler (Laboratoire d'Optique Biomédicale, EPFL, Switzerland). These samples were chosen as representatives of a typical photobleaching conditions in Dreiklang labeled living cells.
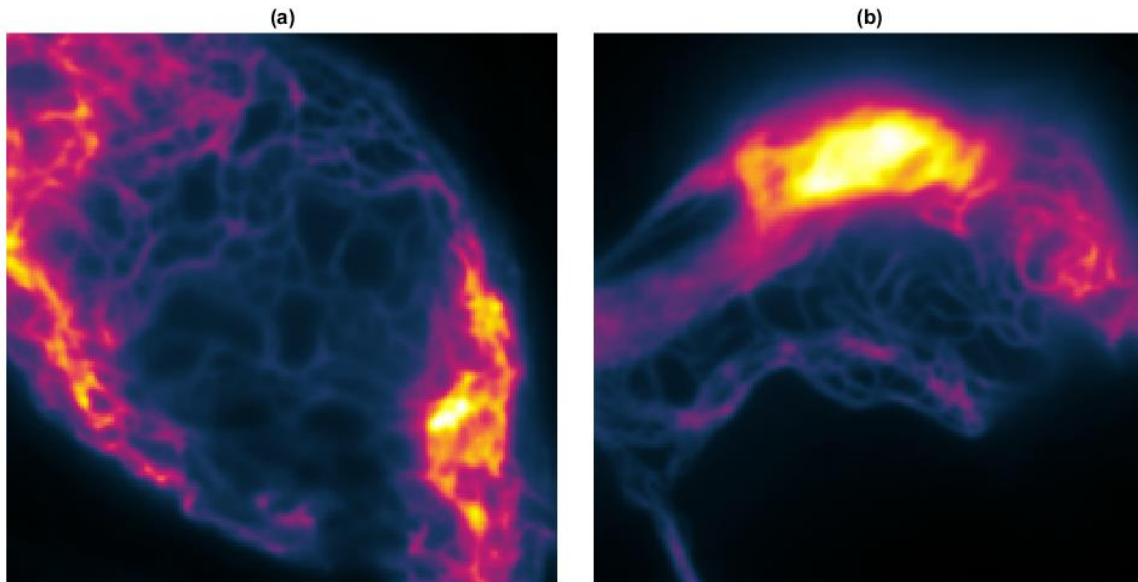

Figure 25 Sample 1 (a), Sample 2 (b) widefield images with morgenstemning colormap [43].

Enhanced SOFI algorithms used in this work where kindly provided by Mr. Tomáš Lukeš (Laboratoire d'Optique Biomédicale, EPFL, Switzerland & MMTG, FEL, ČVUT, Czech Republic). Core of the SOFI image processing algorithm is freely available at [44]. In this work, I developed a novel set of algorithms for bleaching correction written in MATLAB. List of all functions can be found in Appendix B. All codes and MATLAB models can be found on the attached DVD.

SAMPLE PREPARATION

HeLa cells were transfected using FuGENE 6 transfection reagent (Promega). For each 1.5 cm2 well, 2 ml Fugene were incubated in 33 ml OptiMEM Reduced-Serum Medium (Life Technologies) during 5 min before the addition of 0.67 mg of the plasmid pMD-Vim-Dreiklang [45]. The solution then stayed 30 min at RT before it was carefully distributed over the cells. Cells were then put back into the incubator and were left overnight before imaging [23].

MICROSCOPE SETUP

The microscope setup [23] was composed of a 60× water-immersion objective with a numerical aperture of 1.2 (UPLSAPO 60XW, Olympus), a green DPSS laser (MLL-FN-532, 800mW, Roithner Lasertechnik) for excitation and a diode laser (iBeam smart, 405 120mW, Toptica) for reactivation and tuning the blinking rate. Andor (iXon DU 897) EMCCD camera was used for the image acquisition. An additional 365nm LED epi-illumination was used to tune the switching kinetics of the Dreiklang fluorescent protein [45].

BLEACHING CORRECTION IMAGE QUALITY ASSESMENT

In the following chapters, I used 3rd and 4th order SOFI images for comparison of the different bleaching correction algorithms. The 2nd order SOFI images look almost identical regardless of the correction method used in this work. An example of 2nd order SOFI comparison can be found in Appendix A, Figure 59. This approach was used in accordance to the assumption stated in Section 3.3 that higher-order cumulants require more blinking events (longer stacks) to properly construct the higher order SOFI images. Therefore, the difference between the bleaching correction algorithms increases both with the increasing number of images used for the image reconstruction and the SOFI order. The importance of longer sequences for higher SOFI orders can be seen in Appendix A, Figure 58. On the other hand, higher SOFI orders are more sensitive to the input image sequence SNR, which limits the order that can be computed without significant image artifacts.

Moreover, I have decided to omit the deconvolution post processing in order to provide results unaffected by additional processing, which may in some cases create disturbing artifacts (E.g. ringing and noise amplification [46], example is given in Figure 26). Also, a custom colormap has been used [43] to better visualize the final SOFI images.
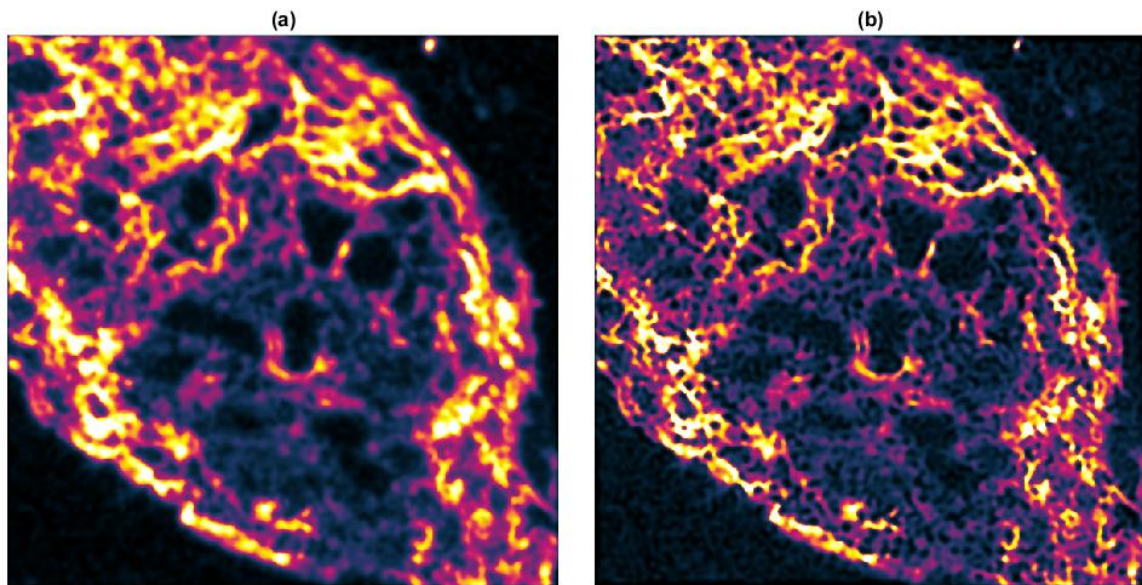

Figure 26 Sample 1, 3rd order SOFI, morgenstemning colormap [43]. Original sample image size 200x200 pixels, 4000 frames, field of view 18.84 μm. Both samples processed with 1st order IIR Butterworth filter with ω_c = 0.01 π rad/sample (discussed later in Section 6.3). Image (a) without deconvolution, image (b) deconvolved with 10-iteration Richardson-Lucy algorithm. (b) Contains unwanted deconvolution artifacts visible both on the cell structure as well as on the "black" background.

6 Results

As was discussed in 3.3, the photobleaching affects the whole Fourier space of the image sequence. According to its exponential characteristics both in time and frequency domains, the photobleaching occurs mostly in the low frequency range (around DC) as higher frequencies of the photobleaching are hidden by the image signal and or white Gaussian noise. In this chapter, I present the results of applying selected digital FIR and IIR filters on the final high-resolution SOFI image. First of all, it is necessary to outline a scheme for rating the impact of a given filter configuration on the time signal.

Figure 27 shows the autocorrelation averaged over all autocorrelation curves calculated by Eq. (36) [31, p. 10] for each pixel time trace in the image sequence. The autocorrelation curves in Figure 27 exhibit an exponential decay where the exponential time constant depends on the average bleaching lifetime.

$$R(\tau) = \int_{-\infty}^{\infty} s(t).s^*(t - \tau)dt \tag{36}$$

As stated in Section 3.1, SOFI assumes that the time signal from each fluorophore is not correlated in time. Assuming high enough sampling (i.e. the acquisition time is shorter than the average on-state lifetime of the fluorophore), we can expect the average autocorrelation function to quickly decrease to zero after $\tau \sim$ blinking period. The bleaching effect introduces a correlation on a longer time scale and influences the expected shape of the autocorrelation function such that the function values are effectively never 0 for $\tau \to N$, where N is the number of acquired frames of the image sequence.
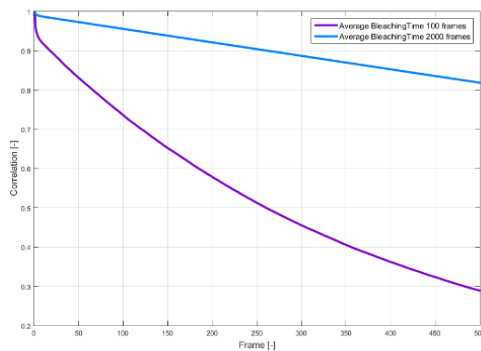

Figure 27 Autocorrelation curves for different bleaching times. Average on-state of emitters: 3 frames. Simulated data set with 3000 frames.
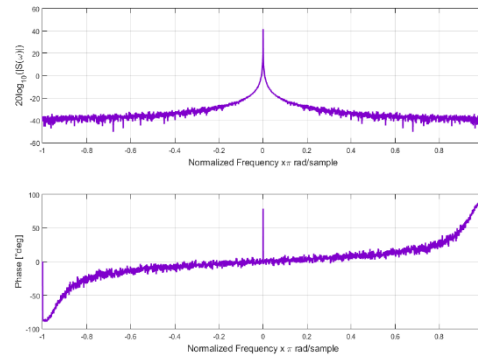

Figure 28 Average PSD (top) from pixel time traces of Sample 1 without bleaching correction and phase spectrum (bottom).

Signal spectrum was introduced in Section 3.3 together with the assumption that the photobleaching can be filtered with a high-pass filter. Figure 28 represents the average PSD of all the pixel time traces in the log-scale calculated from the real Sample 1 in order to show what to expect during filtering in the terms of required attenuation in the stopband and choice of the optimum cut-off frequency. Because of the nature of the random blinking of all the emitters, it is evident from Figure 28 that the most of the PSD o higher frequencies looks like a standard white Gaussian noise. Furthermore, the bleaching effect resides near the zero frequency as expected.

6.1 High-pass FIR

We have discussed the FIR filter design in Section 4.5.1. Unlike the IIR filters, FIRs have a finite impulse response, which means that the filter's impulse response do not affect the time signal if we cut the delay before and after processing. Standard FIR filters tend to have orders of approximately 100. The delay required for the filter to work correctly corresponds to the filter order. Therefore it is sufficient to cut-out about 100 samples that will not be used in further SOFI processing. As mentioned in Section 3, first approx. 50 – 100 images of the image sequence is good to remove. These images can be used to feed the filter in order to avoid artifacts.

There are 3 main parameters for FIR filter design – filter order, cut-off frequency and the window function. All of these parameters affect the autocorrelation function, but sweeping through all of these parameters at once would be inefficient and computationally costly. The general impact of FIR filter order on the autocorrelation function is shown in Figure 29, where we can see, that the lower filter orders are not suitable while too high order filters doesn't have any further impact. In fact, higher filter orders produce an unwanted ripple of the autocorrelation curve.
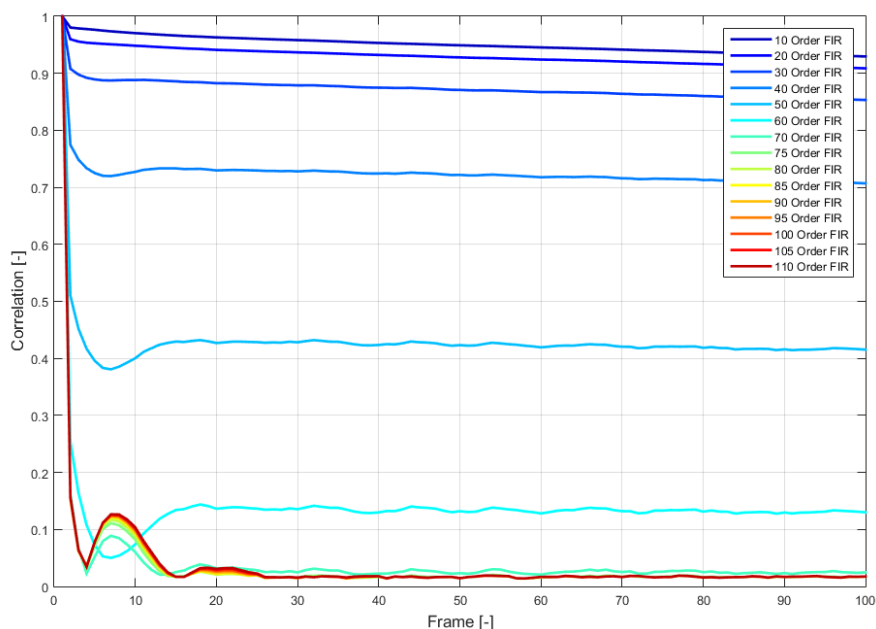

Figure 29 Autocorrelation function after filtration by FIR filters of various orders with normalized ω_c = 0.1 π rad/sample and Hamming window. It is obvious that lower filter orders are not sufficient.

Impact of the window type on the autocorrelation function is illustrated in Figure 30 (a). It is clearly visible, that for a given ω_c = 0.05 π rad/sample, most of the window functions act similarly, excluding the flattop and triangular window functions. In fact triangular and rectangular window functions are rarely used for FIR filter design [47]. The impact of choosing a different cut-off frequency is shown in Figure 30 (b). It is obvious that ω_c modifies the shape of the autocorrelation function.
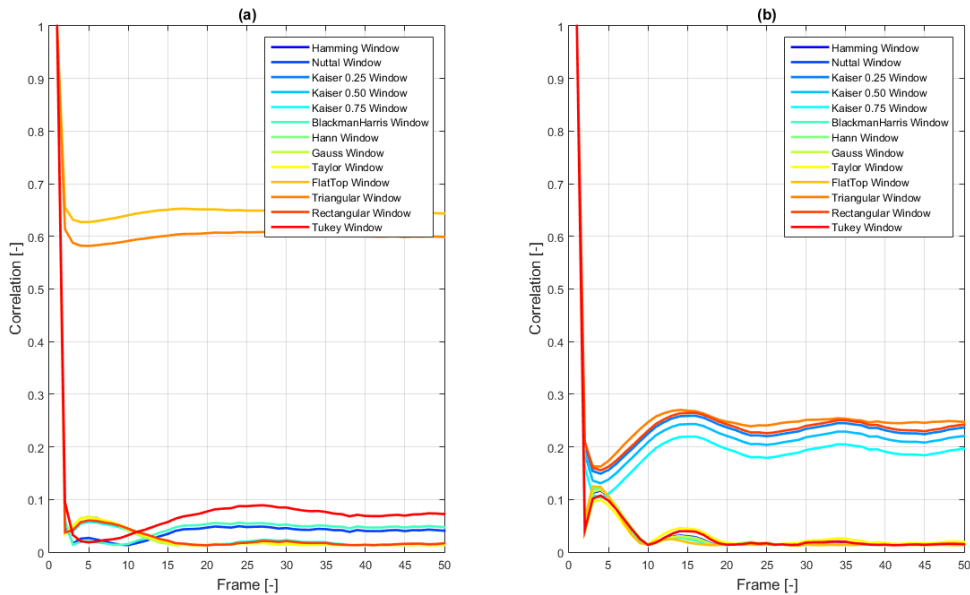
Figure 30 Autocorrelation function after filtration by 100th order FIR with normalized ω_c = 0.05 (a) and ω_c = 0.1 (b) π rad / sample. Filter was customized by several window functions. The triangular window in (a) shows poor performance as was suggested in Section 4.5.1.

Another issue can be caused by the window function. Figure 31 shows the Nuttall and Hamming window FIR designs while keeping the same filter order. The Nuttall window has higher attenuation in the stopband, but also a wider transition band. This is a problem, because in some cases, the filter is unable to reach its maximum attenuation at the DC because of a very low cut-off frequency. The solution is to increase the filter order which however as a feedback creates the unwanted ripple in the autocorrelation function.
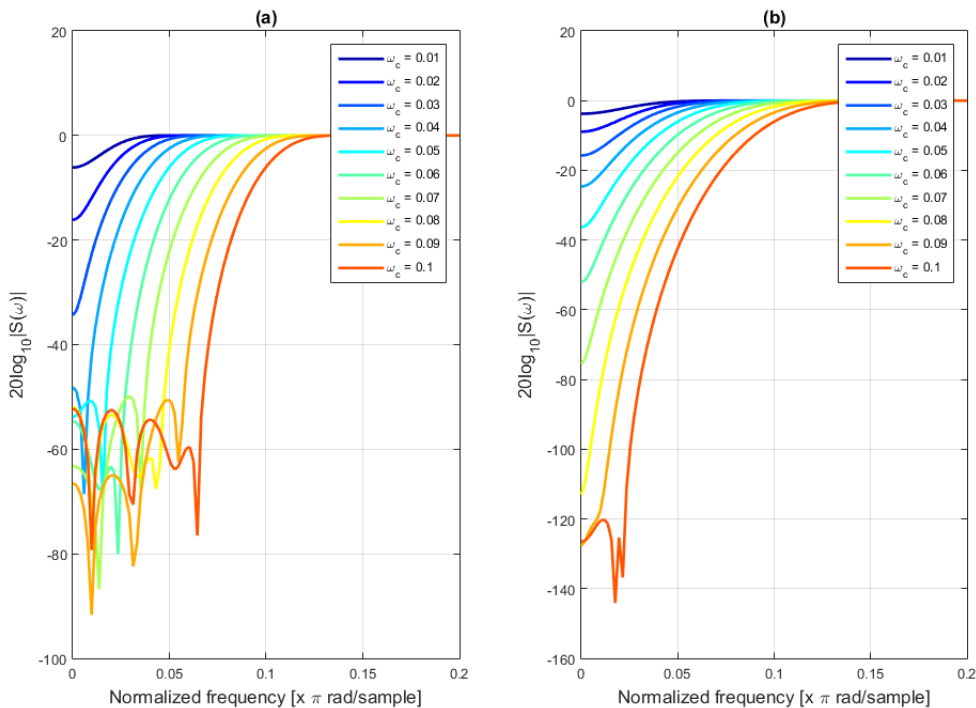

Figure 31 High-pass 100th order FIR filter customized by Hamming window (a) and Nuttall window (b). Decreasing ω_c results in a loss of attenuation of the filter around DC, which in turn has a negative impact on the filtration itself.

The solution is to find a compromise which minimizes the unwanted ripple of the autocorrelation curve and choose either to increase ω_c or filter order. Because increasing ω_c may lead to loss of information, it is recommended to increase the filter's order instead. This can be done in a loop, which

should be stopped once the frequency response reaches a filter's zero. The initial sweep of the best filter parameters can also be reduced to a specific image area in order to speed up the process. I have used an area of 21x21 pixels, selected such that the central pixel was always the brightest one of the widefield image.

Because of the need to sweep through different filter parameters, there should be a method of choosing the optimal configuration. The solution that seems to work best is to use the autocorrelation curve as an optimization criteria. Because bleaching can be understood as a correlation in time, the first attempt is to integrate the function and select the optimal configuration based on its weight. This solution however neglects the ripple, that can be created during filtration as seen for example in Figure 30. To overcome this issue, I have weighted the result by the absolute difference of the local minimum and maximum of $R(\tau)$ further weighted by coefficient α. This operation is represented by Eq. (37) where W_i is the difference of the local minimum and maximum of the function (assuming $W_i \in (0,1)$). Process is graphically shown in Figure 32. The results are further discussed in the next Section.

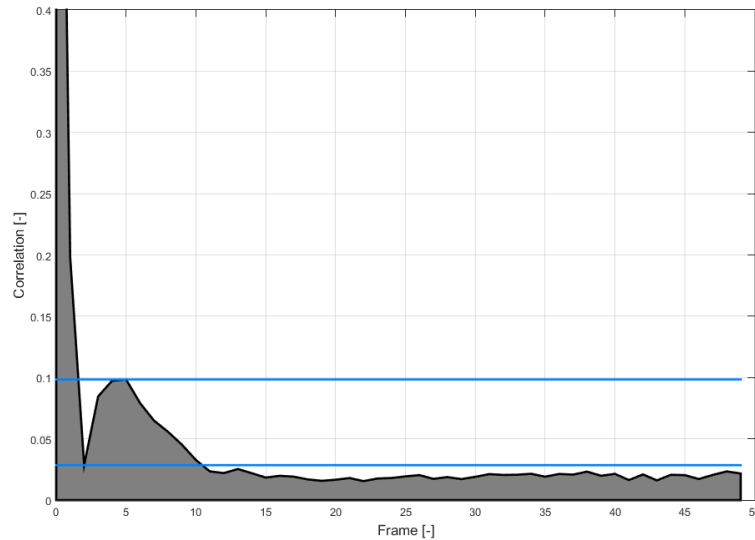$$R_i = \frac{(\alpha W_i + 1)}{N} \sum_{k=0}^{N-1} R_i[k] \tag{37}$$

Figure 32 Demonstration of selection of the best filter parameters based on the shape of R(τ), which is integrated in the selected range and then weighted by |Lmax - Lmin|. The best filter configuration is selected by choosing the minimum value among all the possible results.

This method is also used in Section 6.3 in case of IIR filters. Important thing to note is that the ripple shown in Figure 32 is a result of taking the absolute value of the correlation function. The number of samples to work with doesn't have to include all the time lags, as we can assume, that R(τ) decreases with τ. I have used 50 samples and assigned α constant value of 10, which worked sufficiently well.

Results of high-pass FIR filtering are shown in Figure 33 and Figure 34 in comparison with two state-of-the-art bleaching correction algorithms: the inverse mono-exponential fitting algorithm and a combination of the inverse mono-exponential fitting together with a division into subsequences algorithm (both presented in Section 3.3). A bleaching uncorrected SOFI images are also included in the comparison.
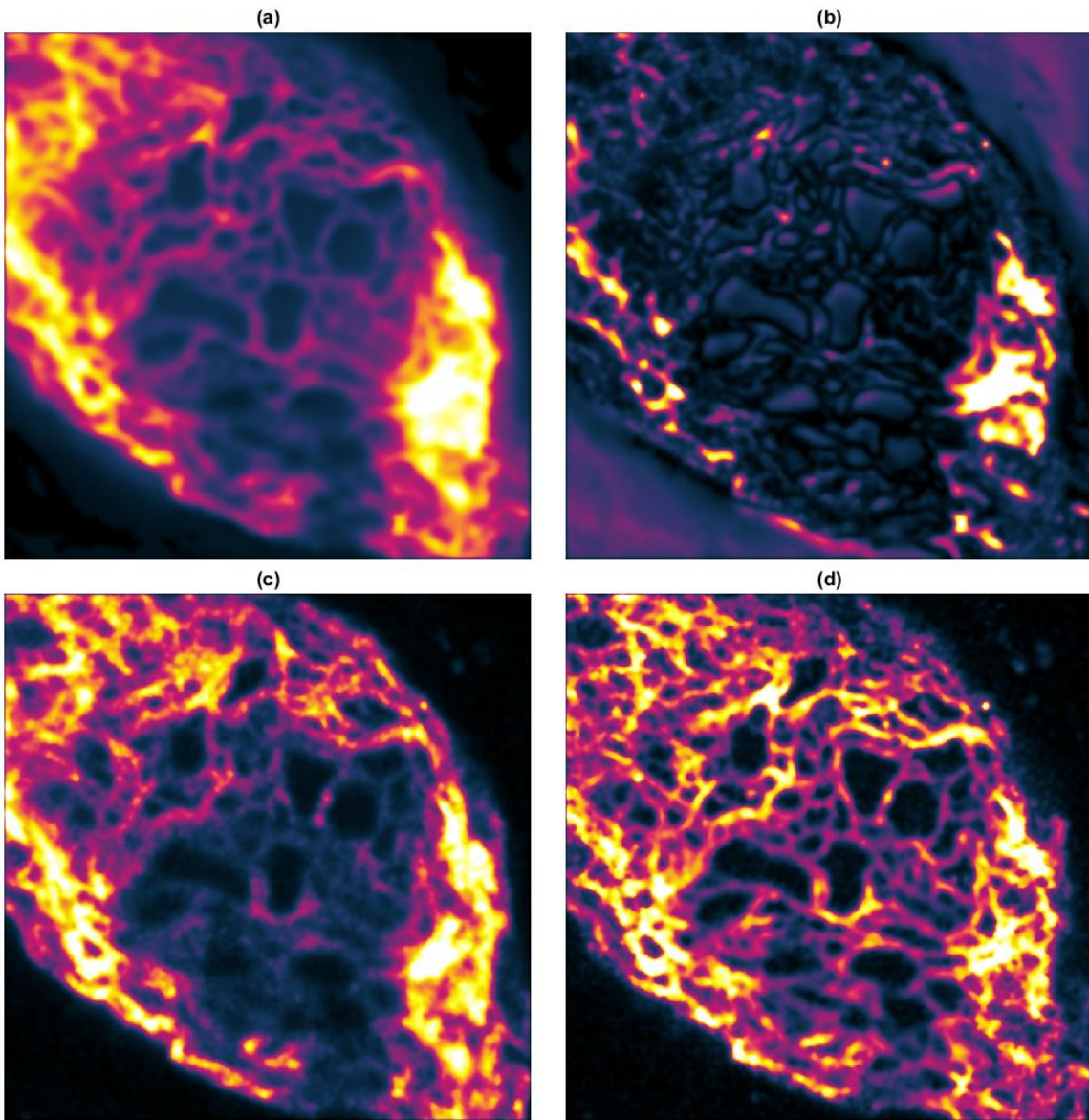
Figure 33 Sample 1. 4th order SOFI Images with morgenstemning colormap [43]. Original image size 200x200 pixels, 4000 frames, field of view 18.84 μm. SOFI image (a) without bleaching correction, (b) with inverse mono-exponential fitting correction, (c) with inverse mono-exponential fitting and division into subsequences correction, (d) with the bleaching correction using filtration with 82nd order high-pass FIR filter, customized by Nuttall window with $\omega_c = 0.1\,\pi$ rad/sample.
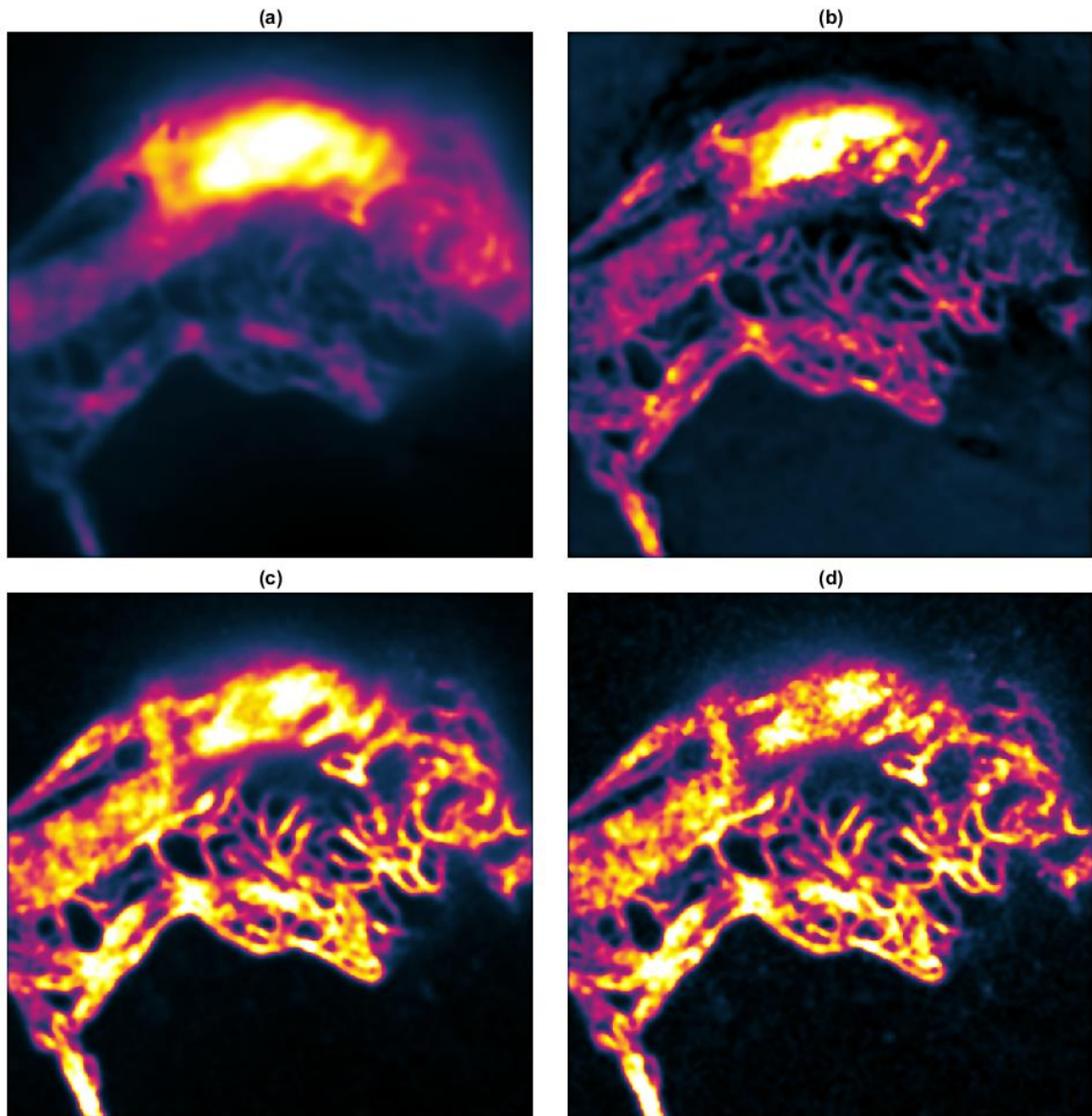
Figure 34 Sample 2. 3rd order SOFI Images with morgenstemning colormap [43]. Original image size 200x200 pixels, 4000 frames, field of view 18.84 μm. SOFI image (a) without bleaching correction, (b) with inverse mono-exponential fitting correction, (c) with inverse mono-exponential fitting and division into subsequences correction, (d) with the bleaching correction using filtration with 82nd order high-pass FIR filter, customized by Nuttall window with $\omega_c = 0.1\,\pi$ rad/sample.

The overall results of correcting the photobleaching with high-pass FIR filtering are visually satisfying. In both cases of the samples used, filtering achieved better image quality than the reference bleaching correction algorithm. On the other hand, this technique requires some sweeping algorithm to select the optimal filter configuration, which is time consuming. Furthermore, as will be discussed in Section 6.3, it is possible to decrease the cut-off frequency for high-pass filtering and potentially gain better results.

6.2 Moving average subtraction

Although the photobleaching effect can be suppressed by high-pass filtering as described in the previous Section, the task can be investigated from a different point of view using low-pass filters. We can assume that our time signals are composed of two parts: the exponential bleaching signal and a superimposed signal coming from the blinking of the emitters. In the first place, it is necessary to determine the photobleaching by calculating the moving average of the image sequence over time.

This process is mathematically described in Eq.(38) Where N is the number of samples used for the averaging [48].

$$y[k] = \frac{1}{N}(x_k + x_{k-1} + x_{k-2} + \cdots + x_{k-N}) \tag{38}$$

Once the bleaching signal is estimated, we can subtract it from the original pixel time trace to obtain the signal "unaffected" by the bleaching. The correction depends on how accurately we are able to extract the bleaching signal which depends on the order of the filter. The process of moving average subtraction is demonstrated in Figure 35.
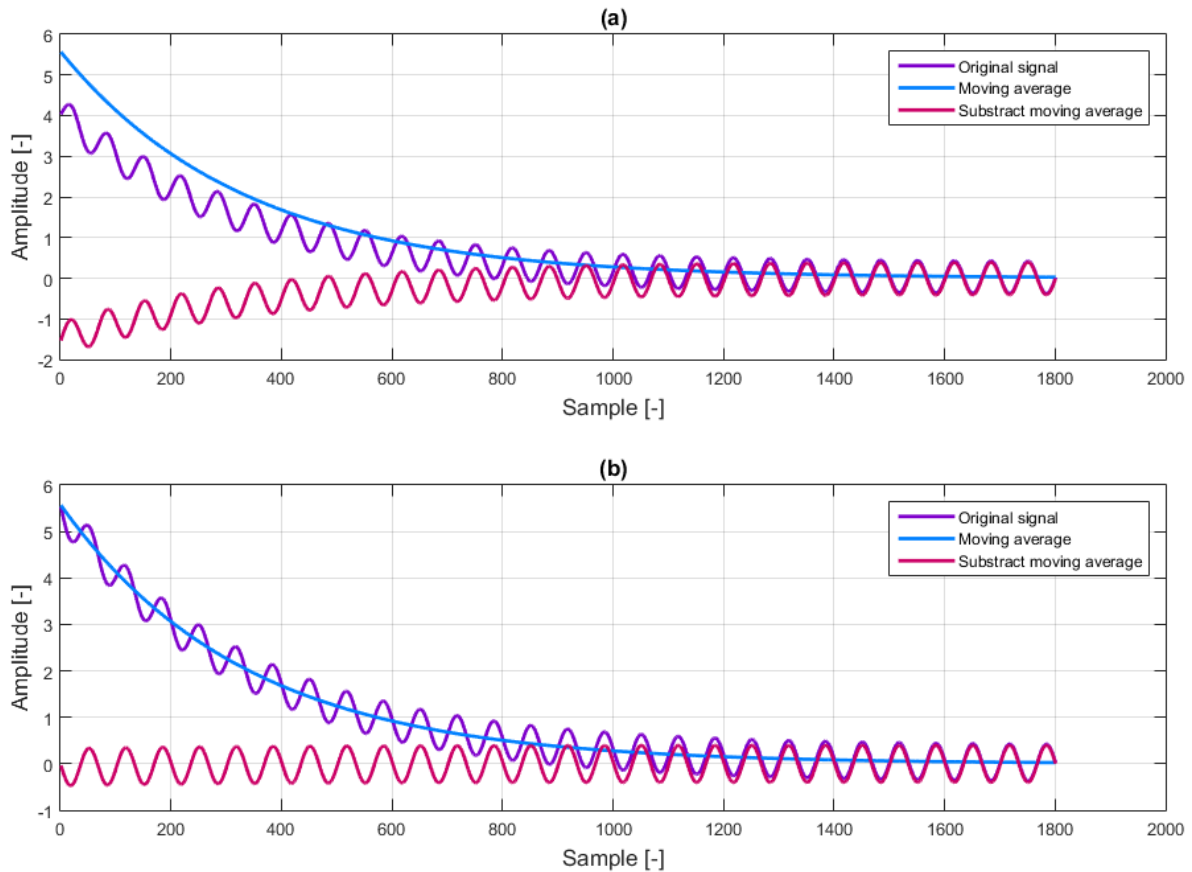

Figure 35 Moving average subtraction. The original signal is modeled as sin(20πt) + exp(-2t). The moving average filter order N is equal to 200. As can be seen in (a),the moving average is delayed behind the original signal causing the negative values in the "subtracted moving average" signal. This problem is solved in (b) by correcting the generated time lag.

The advantage of this implementation is that the moving average can dynamically react on the signal changes. Furthermore, the user can select how many frames at the beginning of the image sequence will be removed (approximately 100 frames at least are recommended). To prove that increasing the filter order provides better results, correlation functions generated by different orders moving average filters were investigated (Figure 36). Figure 37 demonstrates the performance of the 200th order subtract moving average filtration.
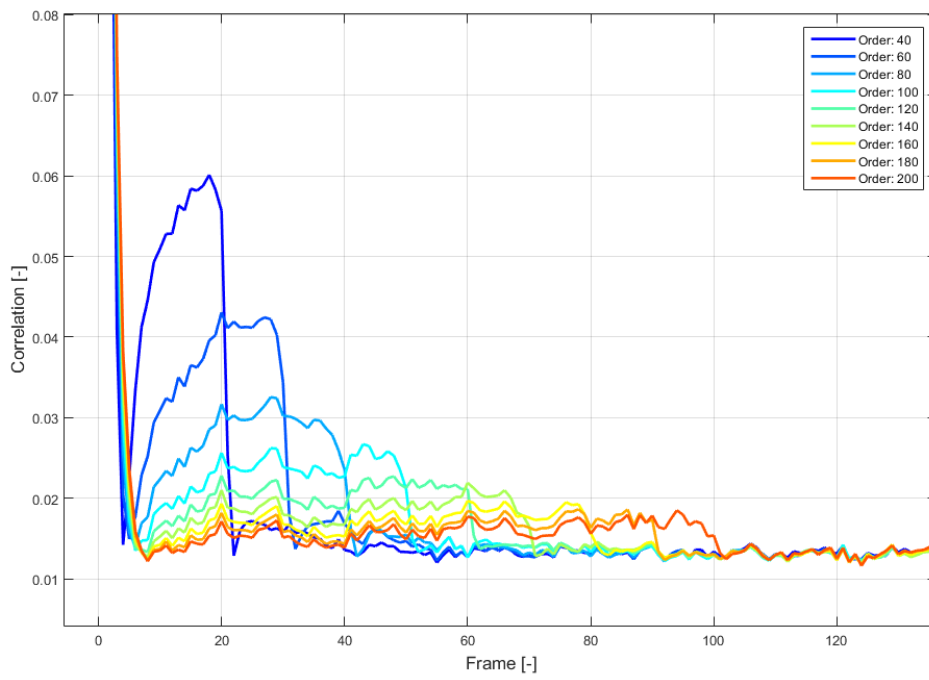
Figure 36 Autocorrelation function after filtration by different order moving average filters. The trend shows that increasing the filter order reduces the overall correlation in time due to photobleaching, which improves the resolution of the final SOFI image.
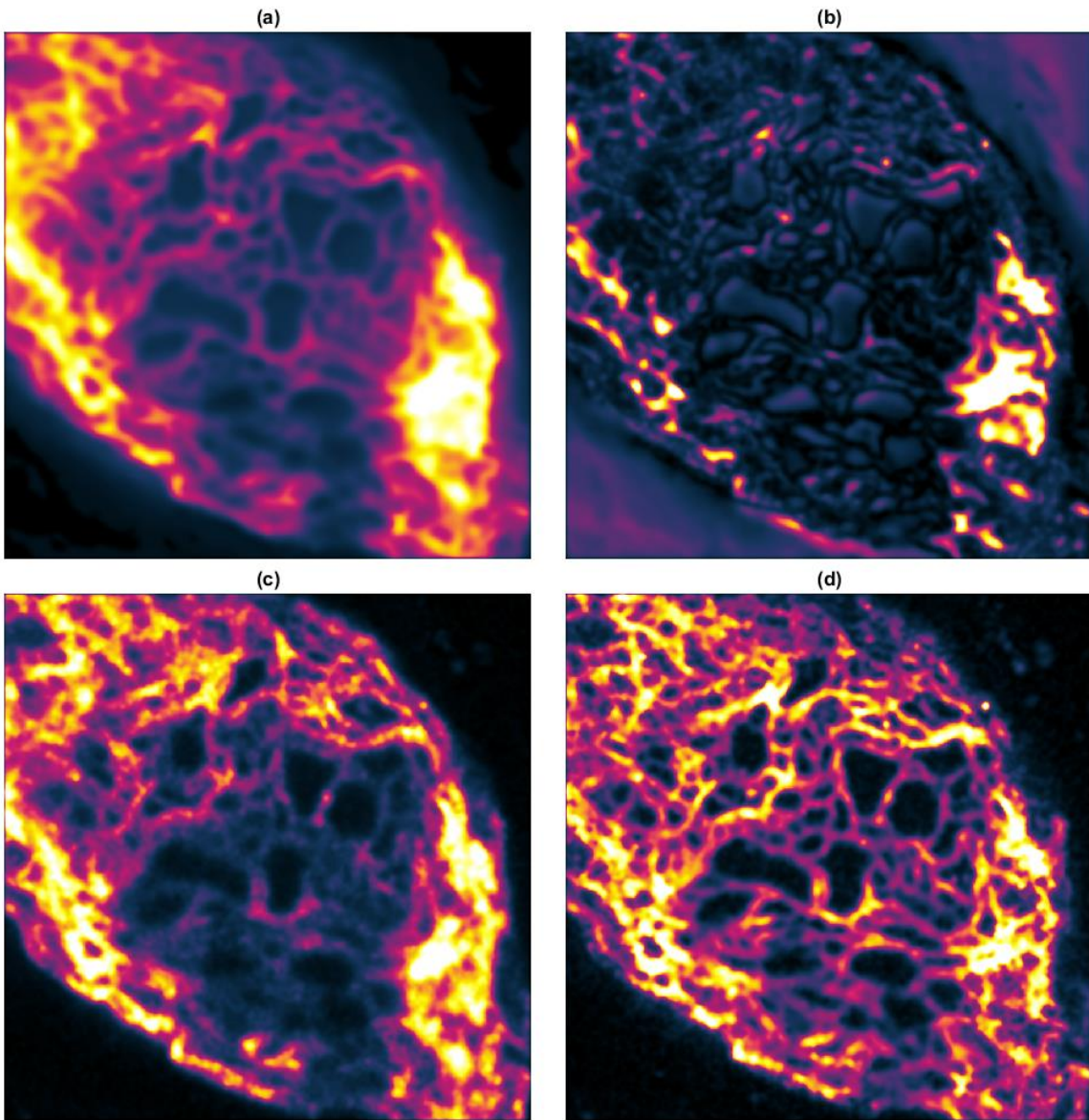
Figure 37 Sample 1.4rd order SOFI Images with morgenstemning colormap [43]. Original image size 200x200 pixels, 4000 frames, field of view 18.84 µm. SOFI image (a) without bleaching correction, (b) with inverse mono-exponential fitting correction, (c) with inverse mono-exponential fitting and division into subsequences correction, (d) with the bleaching correction using the moving average subtraction technique, 300th order.
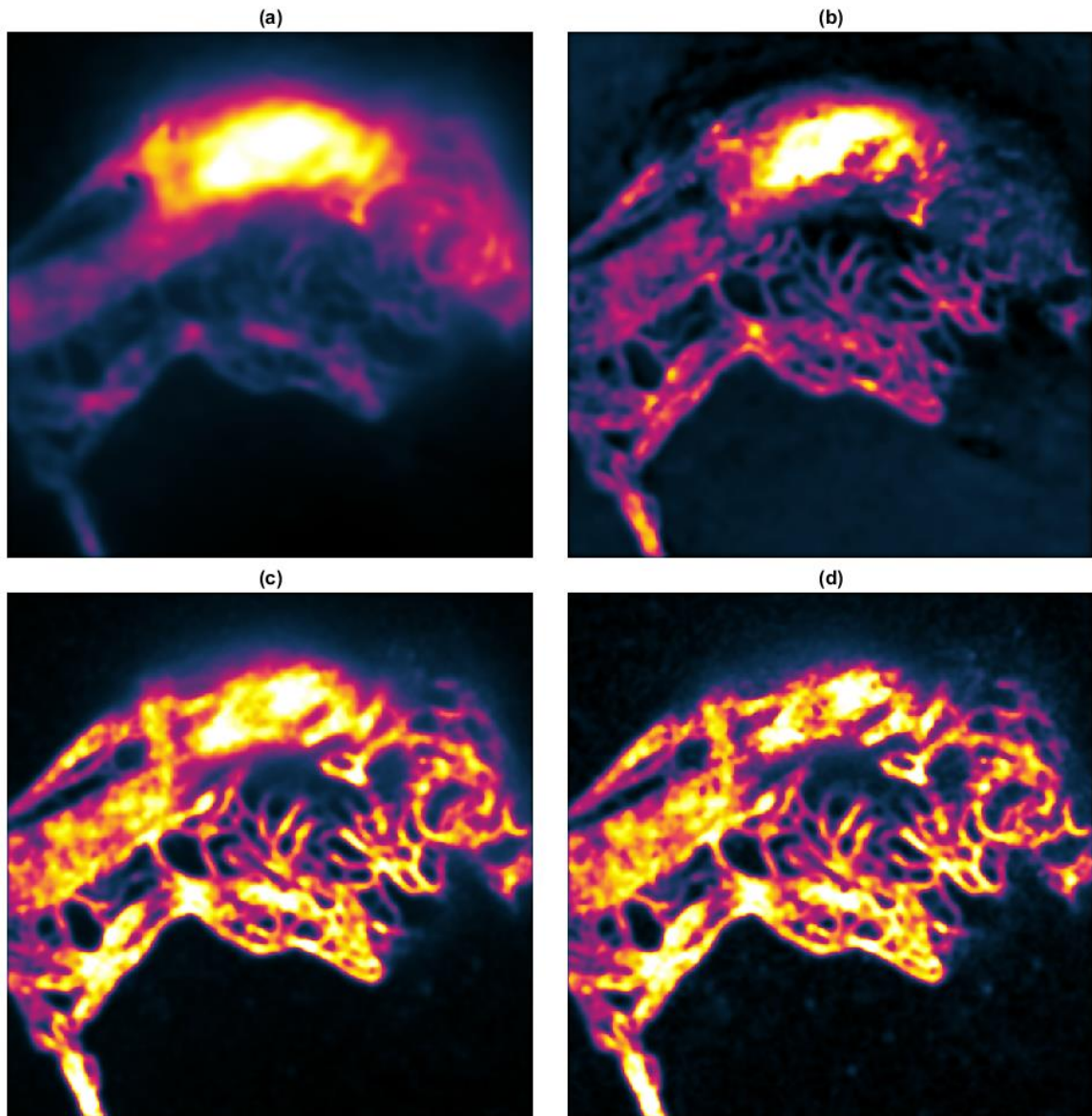
Figure 38 Sample 2. 3ʳᵈ order SOFI Images with morgenstemning colormap [43]. Original image size 200x200 pixels, 4000 frames, field of view 18.84 µm. SOFI image (a) without bleaching correction, (b) with inverse mono-exponential fitting correction, (c) with inverse mono-exponential fitting and division into subsequences, (d) with the bleaching correction using the moving average subtraction technique, 300ᵗʰ order.

The overall resolution improvement factor over the present bleaching correction algorithm can be examined visually (Figure 37 (c), (d)) and (Figure 38 (c), (d)).

6.3 High-pass IIR

IIR filters have advantage over FIR filters with a build-in feedback, allowing them to minimize the transition band while attaining higher attenuation at lower orders. They are ideal candidates for signal filtering. The only problem comes from the IIR feedback and long impulse response. To give an example, we will start with results from Section 6.1, when the ideal cut-off frequency proved to be $\omega_c = 0.07\,\pi$ rad/sample. According to Section 4.5.2, we will further assume standard parameters for passband ripple of 3dB and stopband ripple of 80dB (these parameters will influence only Chebyshev, Inv. Chebyshev and Cauer filters).

Table 1 – Length of the impulse response for different IIR filter types and orders.

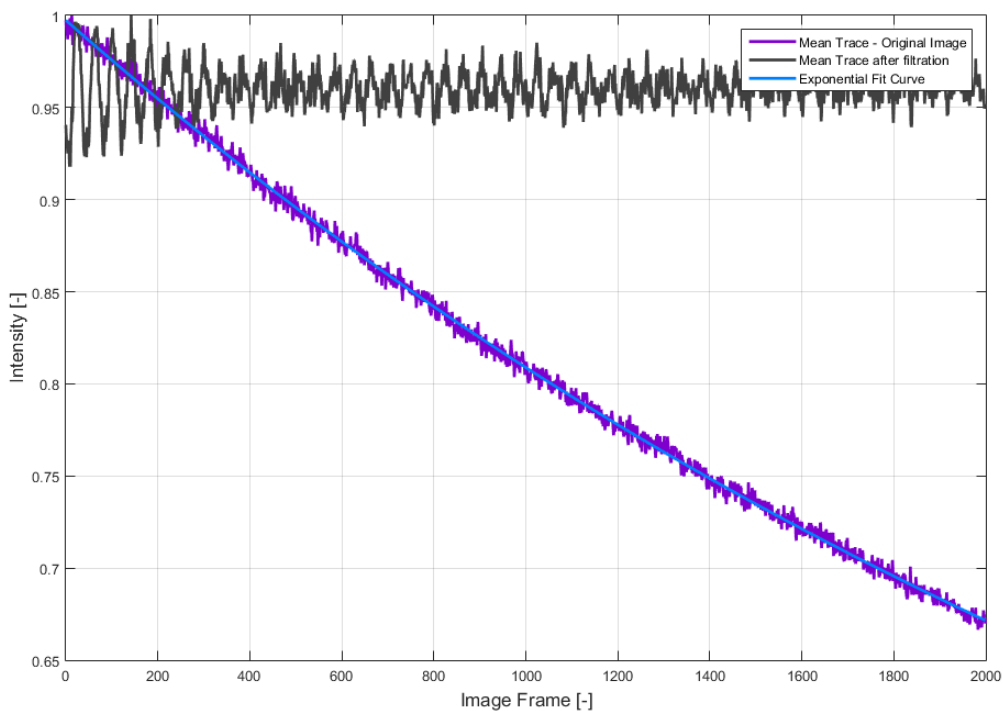| Order [-]	Butterworth [Samples]	Chebyshev [Samples]	Inv. Chebyshev [Samples]	Cauer [Samples]
1	44	44	44	5466
2	63	99	54	99
3	90	255	19	257
4	118	481	27	500
5	146	775	46	867
6	175	1134	74	1434
7	203	1559	109	2324
8	232	2050	151	3732
9	261	2606	199	5970
10	290	3228	253	9531

Figure 39 Mean trace (dark grey) after filtration by 10th order Cauer filter with ω_c = 0.05 π rad/sample showing artifacts in time signal caused by long impulse response of the filter.

Table 1 shows that increasing filter order results in longer impulse response as in the case of FIR filters, the dependence is however not linear. Given a sequence of 10 000 image frames for SOFI processing and using the 10th Cauer filter would result in a total loss of 9500 samples which is unacceptable. Using this filter without removing the samples affected by the filter's impulse response will inevitably result in creation of signal artifacts shown in Figure 39. On the other hand Cauer filters usually do not need such high orders and one can be easily satisfied with order ranging from 3 to 5 which results in a loss of 250 – 850 frames. The Chebyshev filter, although having a shorter response than Cauer, has still a very long impulse response. Figure 40 summarizes how the filter and its order affects the autocorrelation function. The inverse Chebyshev filter (c) performed at worst and can be omitted from additional considerations. It can be also deduced, that IIRs do not need high filter orders and in fact, the best results are obtained for the 1st filter order. We can also expect the shape to vary for different cut-off frequencies. Additionally, we can see, that highest autocorrelation ripples occur for the Chebyshev (b) and Cauer (d) filter results, which favorites the Butterworth IIR filter (a).
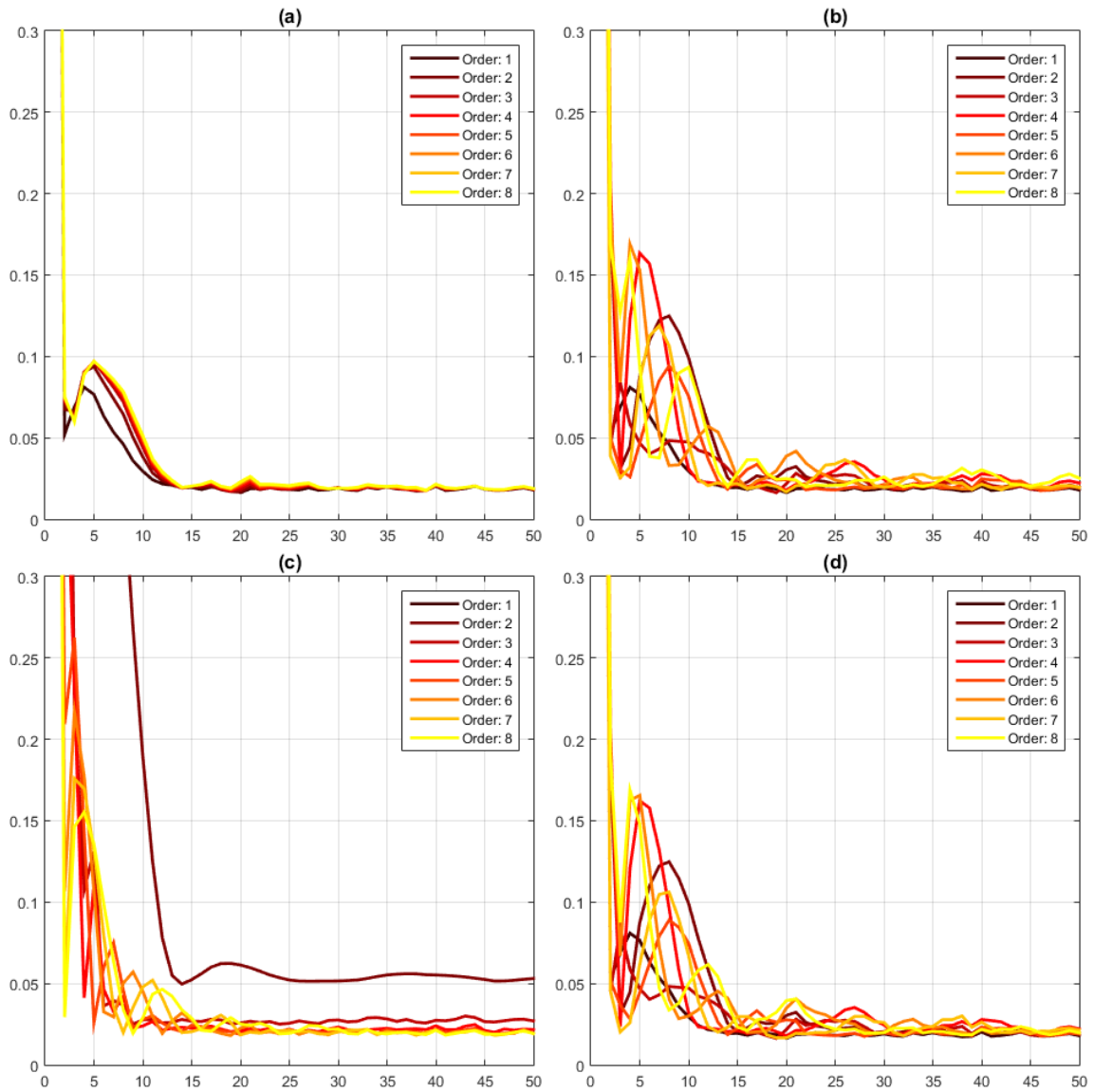
Figure 40 Autocorrelation functions of Sample 1 filtered using different order IIR filter types. Butterworth (a), Chebyshev (b), Inverse Chebyshev (c) and Cauer (d). All filters have the same cut-off frequency of 0.07 π rad/sample. Pass ripple used: 3dB, stop ripple used: 80dB. Colormap: hot. Frame indexes on the X - axis, autocorrelation function values on the Y-axis (removed from charts for better visibility).

Because we have omitted the inverse Chebyshev filter and assumed the optimal IIR filter order to vary around 1, we can create a function to sweep though all of these parameters (Including ω_c ranging from 0.01 to 0.1 π rad/sample) and select the optimal configuration for filtration. The automatic filter selection is based on Eq. (37) and its results are shown in Figure 41 for remaining filter types (Butterworth, Chebyshev and Cauer) and orders of 1 and 2. Legends have been removed due to the higher amount of curves in the chart.
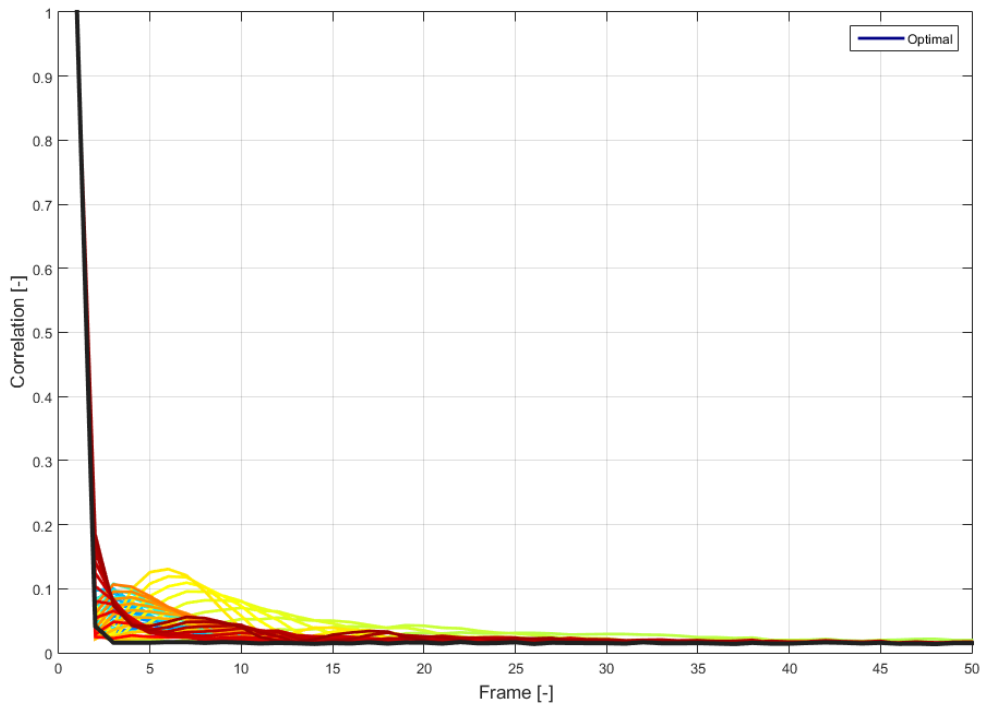
Figure 41 Parameter optimization. Sweep though Butterworth, Chebyshev and Cauer filter parameters with orders ranging from 1 to 3 and 10 ω_c linearly deployed in range from 0.01 to 0.1 π rad/sample. Automatic (optimal) curve is highlighted with dark grey color (Butterworth 1st order with ω_c = 0.01 π rad/sample).

The best filter that creates a ripple-free autocorrelation function is the Butterworth 1st order IIR filter with the lowest cut-off frequency possible. This attribute is also very important, as it means, that almost none of the useful information is being filtered away. However, there is still one more thing to consider when specifying low cut-off frequencies for filter design. It is the length of the impulse response. Various cut-off frequencies for the filter design are depicted in Figure 42 along with the corresponding frequency characteristics and the impulse response length.
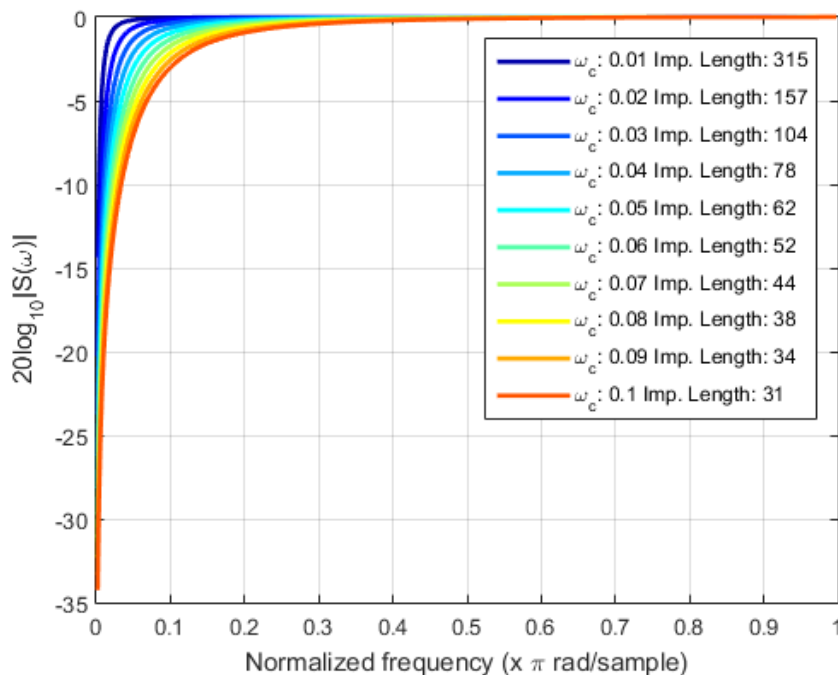

Figure 42 1st order Butterworth IIR filter with different ω_c ranging from 0.01 to 0.1 π rad/sample showing the increasing length of the impulse response of the filter with decreasing ω_c .

We can further investigate the function of the filter by looking at the Butterworth filter coefficients and into the MATLAB documentation (function "filter"). Regardless of the ω_c, the filter has 4 coefficients: a_0, a_1, b_0, b_1. According to the MATLAB documentation, the differential equation is:

$$a_0 y(k) = b_0 x(k) + b_1 x(k-1) - a_1 y(k-1) \qquad (39)$$

According to Eq. (39), the filter has a single feedback and one delay block. The filter structure is shown in Figure 43 and corresponds to the structure of a DC-blocking filter from [49] in case of $b_0 = 1$ and $b_1 = -1$. Both the Butterworth 1st order filter and the DC blocking filter from [49] perform almost the same with just minor differences.
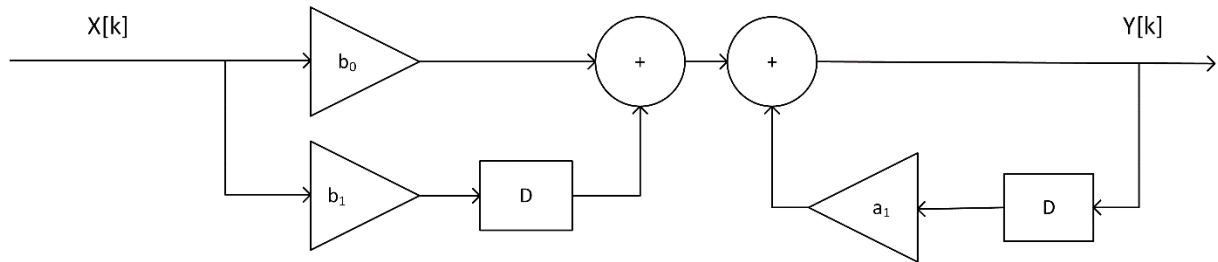

Figure 43 Butterworth 1st order filter structure with single feedback (a$_1$ coefficient). a$_0$ was used for normalization only.

In other words, the optimal filter is in fact a DC-blocking filter. The result of photobleaching correction with the IIR DC-blocking filter is shown in Figure 44 and Figure 45.
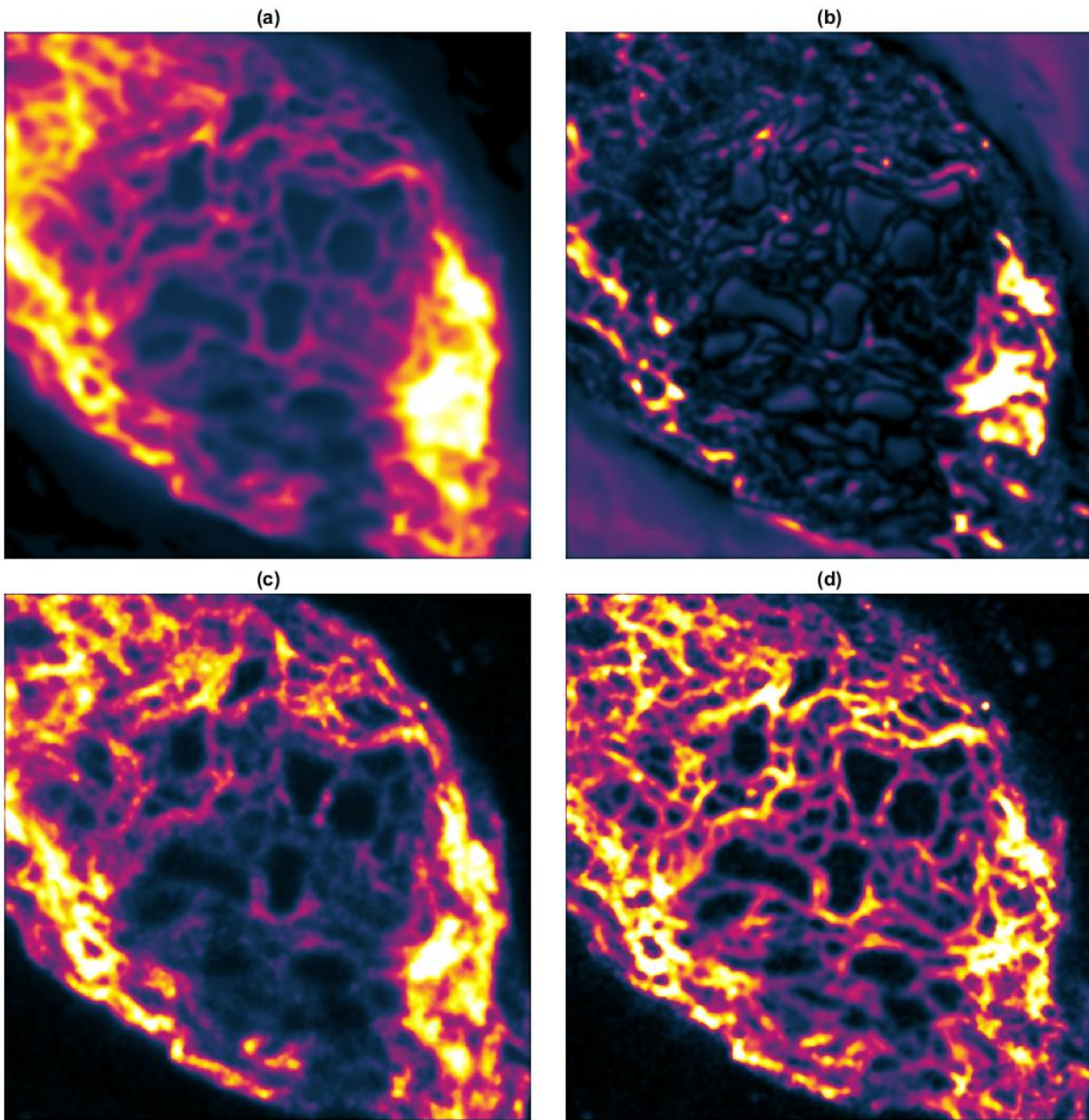
Figure 44 Sample 1. 4th order SOFI Images with morgenstemning colormap [43]. Original image size 200x200 pixels, 4000 frames, field of view 18.84 μm. SOFI image (a) without bleaching correction, (b) with inverse mono-exponential fitting correction, (c) with inverse mono-exponential fitting and division into subsequences correction, (d) with the bleaching correction using filtration with 1st order high-pass IIR Butterworth filter with ω_c = 0.01 π rad/sample.
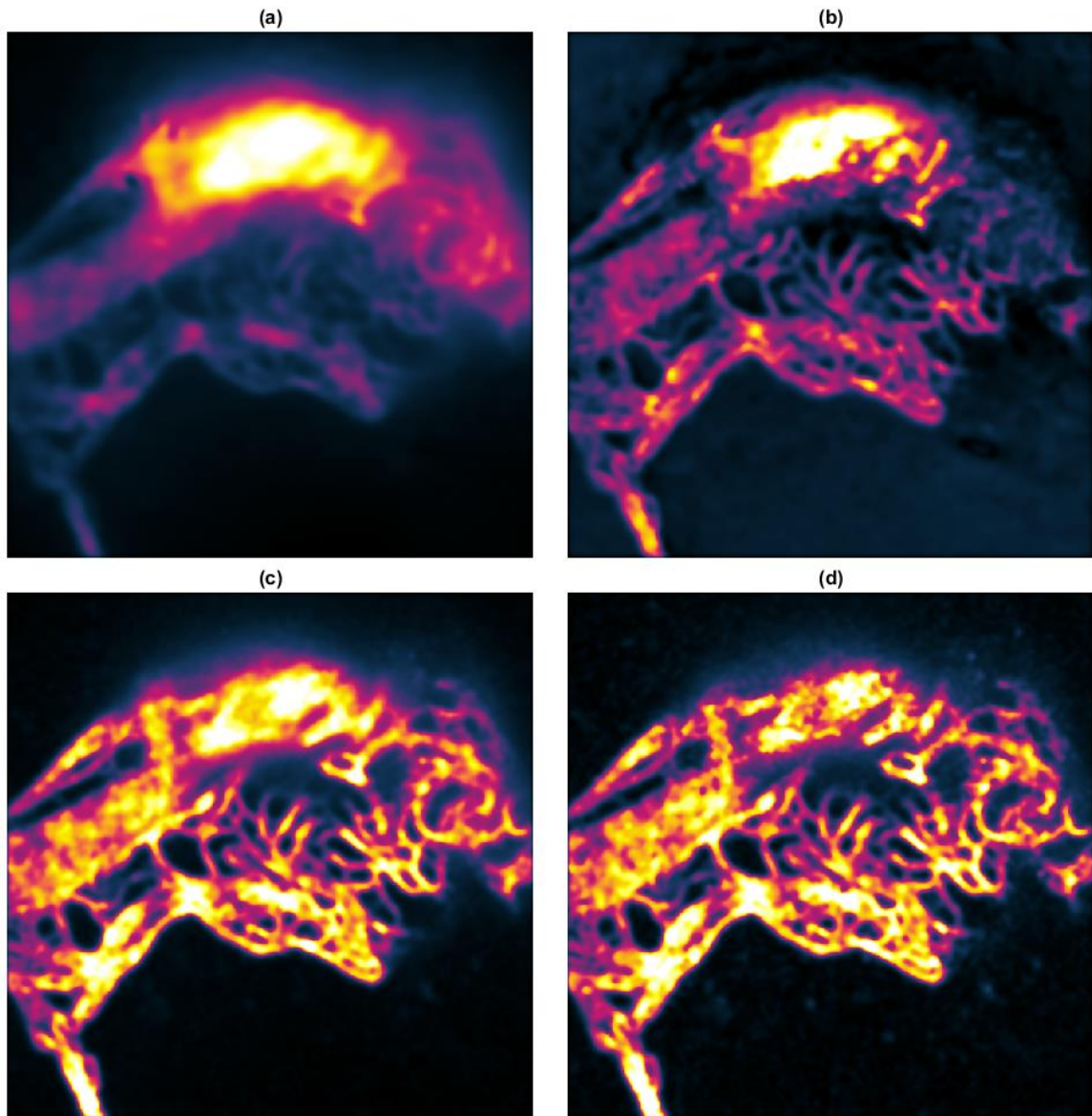
Figure 45 Sample 2. 3rd order SOFI Images with morgenstemning colormap [43]. Original image size 200x200 pixels, 4000 frames, field of view 18.84 μm. SOFI image (a) without bleaching correction, (b) with inverse mono-exponential fitting correction, (c) with inverse mono-exponential fitting and division into subsequences correction, (d) with the bleaching correction using filtration with 1st order high-pass IIR Butterworth filter with ω$_c$ = 0.01 π rad/sample.

We can see, that filtration with IIR 1st order Butterworth filter is an efficient way of correcting the photobleaching. Optional sweep through the filter's ω$_c$ can be performed, but in most cases, choosing either 0.01 or 0.02 π rad / sample will probably yield the best results. Additional speculations about using different IIR filters can be closed by comparing frequency responses of 1st order Chebyshev and Cauer filters with the Butterworth while keeping the same cut-off frequency. This is shown in Figure 46. All frequency responses are identical. Therefore, any of the 3 IIR filters can be used for bleaching correction. From now on, the Butterworth filter was used for simplicity of the filter design.
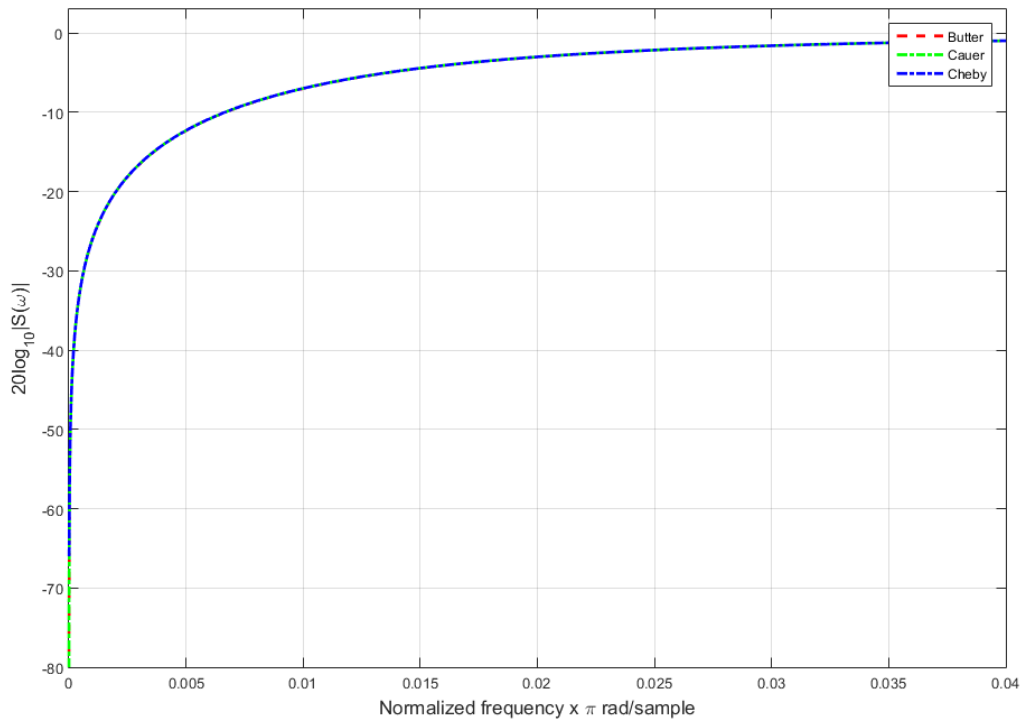
Figure 46 Frequency responses of Butterworth, Chebyshev and Cauer filters of the 1st order with ω_c = 0.02 π rad/sample.

6.4 Bank of filters

So far, I assumed, that low frequencies do not contain any useful information, which may not be always true. In that case, filtering with a high-pass filter would result in a loss of information and reduction of the final SOFI image resolution. To deal with this fact, I have designed several filter banks to decompose the time signal from all pixels into corresponding number of sub bands and then process these signals to gain insight of what the sub bands are composed of. Among all the available filter banks compositions, I have selected these:

- Symmetric tree filter bank with decimation [50] - Figure 47
- Asymmetric tree filter bank with decimation [50] - Figure 48
- Standard filter bank with multiple band-pass filters - Figure 49

In case of the symmetric tree filter bank, the signal is filtered both with low-pass and high-pass filters (assuming FIR filters in our case) and then decimated by 2. The cut-off frequency must be equal to 0.5 π rad/sample in order to avoid aliasing after the decimation. In the next step, both signals are separately filtered by the same filters and then again decimated by 2, which results in 4 signals with ¼ length of the original one. In the following steps, the amount of band-pass signals will be always multiplied by a factor of two. This technique is efficient for processing signals with high initial sampling rate and computing demands on the processing since the band-pass signals have lower sampling rate. The band-pass signals can be up-sampled and joined together under special (perfect reconstruction) conditions. More details about sub band decompositions can be found in [32, p. 133] , [29, pp. 296-302] and [51, pp. 143-195].
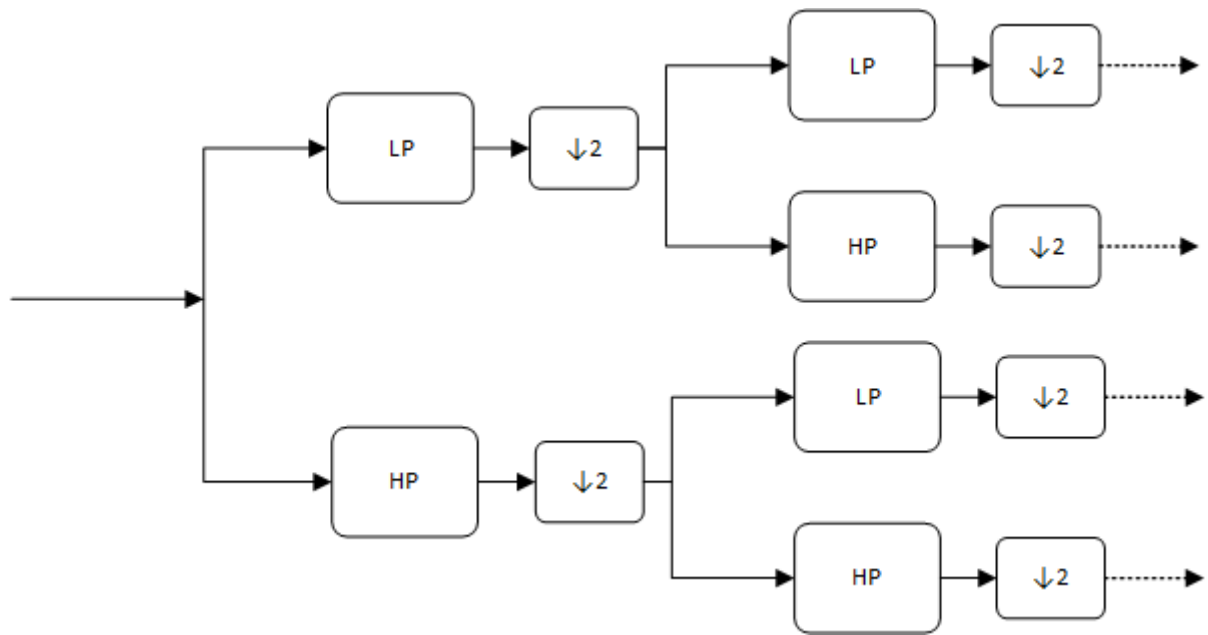
Figure 47 Symmetric 2^N filter bank with decimation by 2 and decomposition into 4 sub bands.
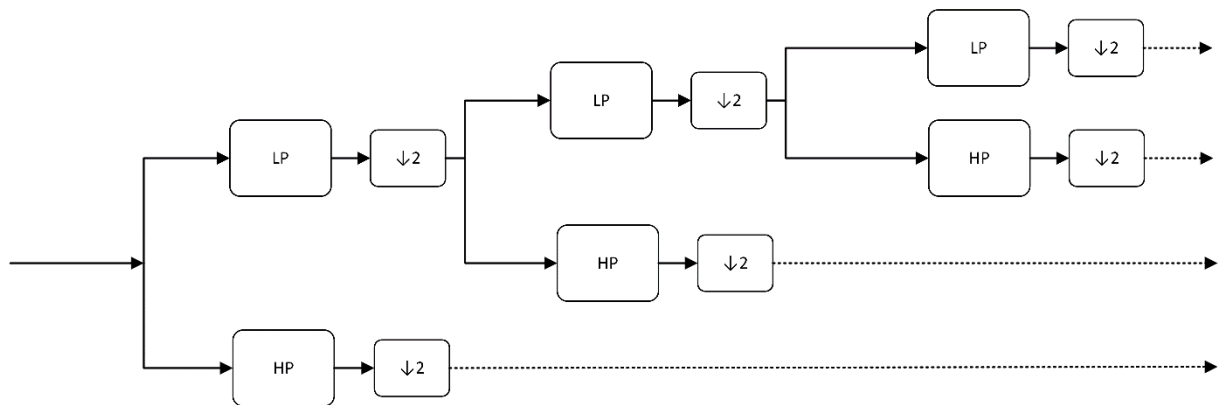

Figure 48 Asymmetric filter bank with decimation by 2 and decomposition into 4 sub bands.

In the second place, the asymmetric tree filter bank can be constructed in 2 ways (always decompose the LP or HP in every step). In the structure showed in Figure 48, I chose to decompose the LP because bleaching occurs on lower frequencies. The signal is also decimated by a factor of 2 after each section and the principle of decomposition is similar to the symmetric tree decomposition. The advantage of the asymmetric filter bank is in the fact that it needs less sub bands in order to detect bleaching within the lowest sub band. Both methods however add filter's impulse response artifacts into the tested sub bands. This is simply caused by the fact that the signal is being filtered multiple times during decomposition. This problem is not very important in real-time applications, but may become serious in post-processing [51]. Methods such as circular convolution or symmetric reflection can be used to solve this, but a much easier method is proposed here. The proposed method includes a one-time signal filtering only that can be taken into account by removing the samples affected by the filter's impulse response. Instead of dividing the spectrum into lower and upper parts as in the case of tree decomposition, the spectrum is divided into several sub bands i.e. the same signal is filtered multiple times by different band-pass (FIR) filters. The scheme of frequency division is depicted in Figure 49. Optionally, the first filter can be designed as a low-pass and the last one as a high-pass filter instead of all being only band-pass.
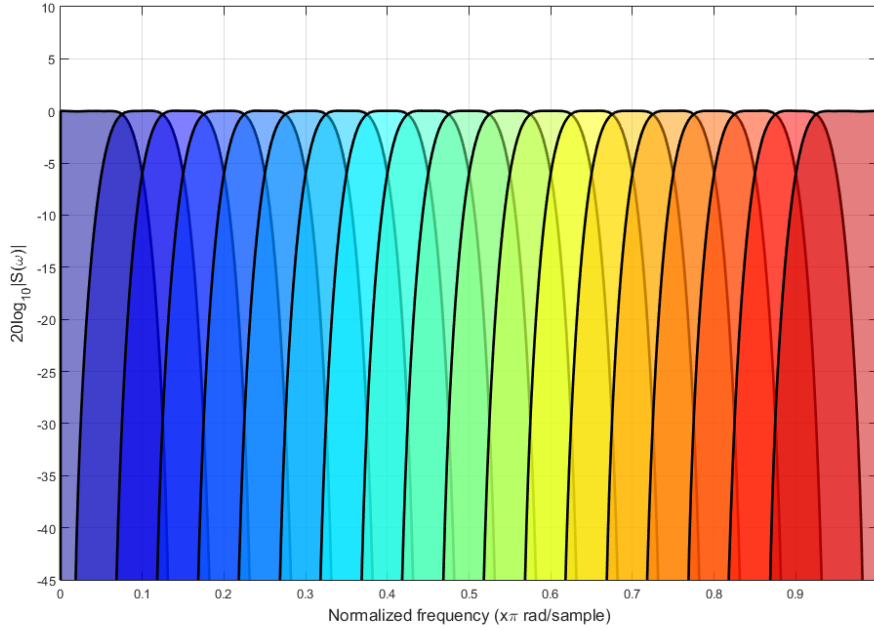
Figure 49 Bank of 19 100th order FIR filters with normalized bandwidth (BW) = 0.1 π rad/sample and overlap of 0.5BW. The first filter is designed as a low-pass and the last one as a high-pass.

Given N different signals from N different band-pass filters, we can compute N high-resolution SOFI images using standard algorithms. Merging these images can be done in several ways, including standard averaging. This might however lead to a situation, where one will combine SOFI computed from a sub band corrupted by bleaching and even giving it the same weight as other non-corrupted images from other bands. Some weighting is therefore needed. I have used similar weights as in the case of Eq. (37) :

$$W_i = \frac{1}{\sum_{k=0}^{N-1} R_i[k]} \tag{40}$$

Eq. (40) represents an inverse integral from the autocorrelation function within a defined area of N frames. The inversion in Eq. (40) is important, because the integral from the correlation curve of an image, affected by photobleaching is always larger than from an unaffected image. The disadvantage of the application of the filter bank is an increased computational demand. The growth is O(n), effectively increasing the computing time N times. The results obtained by these methods (Figure 50) provides worse results compared to previously proposed approaches and the application of filter banks for photobleaching correction is not recommended.
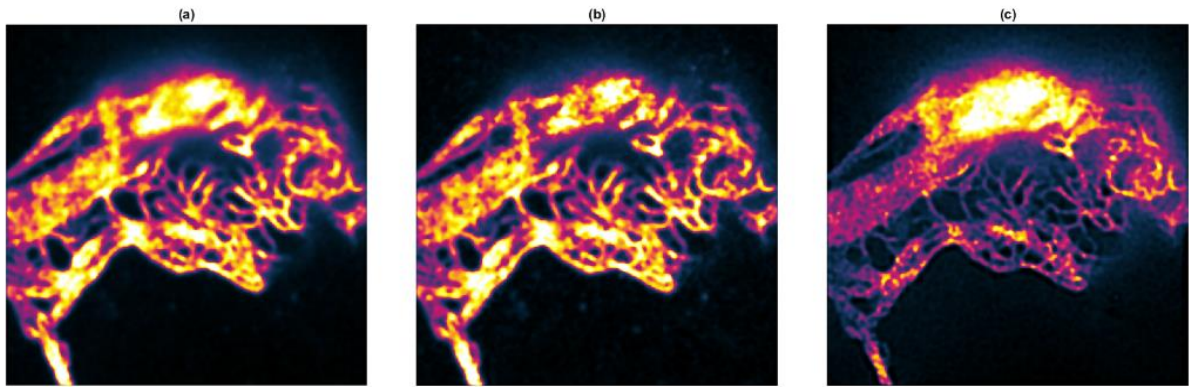
Figure 50 Sample 2. 3ʳᵈ order SOFI Images with morgenstemning colormap [43]. Original image size 200x200 pixels, 3000 frames, field of view 18.84 μm. SOFI image (a) with inverse mono-exponential fitting and division into subsequences correction, (b) with the bleaching correction using 1ˢᵗ order IIR Butterworth filter with ω_c = 0.01 π rad/sample, (c) with bleaching correction by a bank of 9 band-pass filters with normalized BW = 0.2 π rad /sample and overlap of 0.5 BW. Used weights for SOFI image merging are available in the following table.

Table 2 Weights for the final SOFI image merging from filter bank. First row represents sub band ID.

1	2	3	4	5	6	7	8	9
0,015	0,118	0,12	0,119	0,137	0,12	0,121	0,12	0,131

We can see, that the weights in Table 2 are similar except for the lowest band, which is an expected result since it's most likely affected by photobleaching. On the other hand, if we compare the results from Figure 50, the basic IIR filtration (b) is still more efficient and 9 times faster. Increasing the amount of band-pass filters would only result in a higher computing demands, not in an improved image quality. The choice of filter bank is also irrelevant.

7 Discussion

OPTIMAL FILTER SELECTION

As discussed in Section 6.1, the optimization procedure for selecting the best filter configuration is based on the shape of the absolute value of the normalized autocorrelation function. The coefficient alpha in Eq. (37) was set to 10. Although this approach has proved useful, there might be other solutions based on the shape of the PSD or including a dynamic autocorrelation peak weighting. Such filter optimization methods could be investigated in the future research.

DENOISING

We can assume, that the fluorescence intensity of the observed sample decreases in time because of the photobleaching. As a consequence, the signal's SNR decreases, causing the images to contain lower levels of the useful signal. Therefore, I have also tested a basic noise removal algorithm – Wiener filtration. This methods calculates the local mean value Eq. (41) and variance Eq. (42) in the N-by-M neighboring area around each pixel. These estimates are then used for pixel wise filtering Eq. (43) [52].

$$\mu = \frac{1}{NM} \sum_{i=1}^{N-1} \sum_{j=1}^{M-1} a(i,j) \tag{41}$$

$$\sigma^2 = \frac{1}{NM} \sum_{i=1}^{N-1} \sum_{j=1}^{M-1} a^2(i,j) - \mu^2 \tag{42}$$

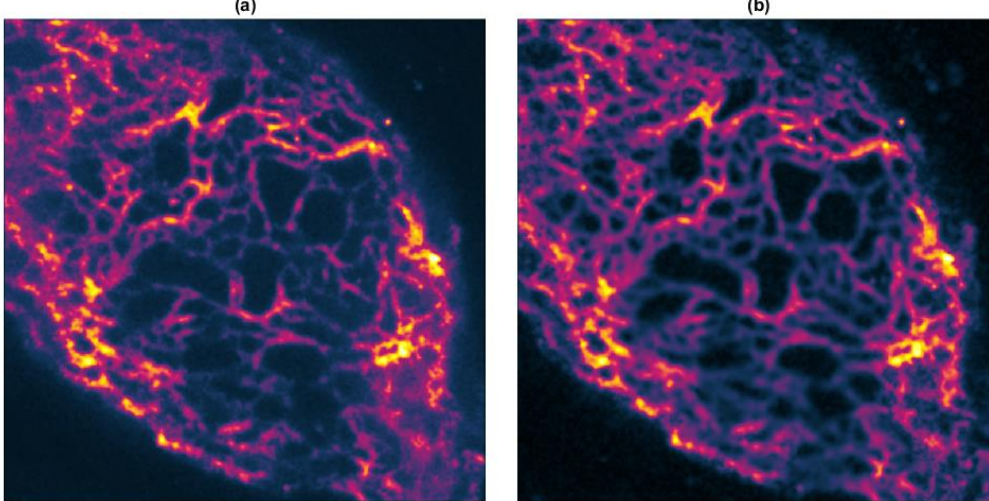$$b(i,j) = \mu + \frac{\sigma^2 - v^2}{\sigma^2}(a(i,j) - \mu) \tag{43}$$

Figure 51 Sample 1. 4ʳᵈ order SOFI Images corrected with Butterworth 1ˢᵗ order IIR filter with ω_c = 0.01 π rad/sample. Original image size: 200x200 pixels, 4000 frames, field of view 18.84 μm. SOFI image (a) without application of the adaptive Wiener denoising filter, (b) with the application of the adaptive denoising Wiener filter.

Figure 51 shows an application of a Wiener denoising algorithm that improves the quality of the image. The investigation of additional denoising preprocessing algorithms might be a subject of a future study.

BANK OF FILTERS

Although bank of filters proved not to be as efficient as a simple moving average subtraction algorithm or IIR DC-blocking filter, it can be eventually used for detection of signals within specific sub bands. This may for example include slow motion molecule drifts. The usage of the tested filter bank is however not recommended for the bleaching correction.

8 Conclusion

Digital filtering for photobleaching correction was investigated using broad range of filters and parameter settings. The bleaching correction algorithm based on 1st order IIR Butterworth high-pass filtering and the moving average subtraction algorithm provided the best results. Regarding the experimental results, the proposed moving average subtraction algorithm was proved to be the most efficient for bleaching correction due to its simplicity and robustness. This algorithm was compared to the state-of-the-art methods with inverse mono-exponential fitting correction and provided visually superior results.

For a special cases like for instance image sequences where the mean trace contains steep intensity variations due to illumination changes, the IIR filtration can provide an advantage. In that case, the filter should be designed as the high-pass 1st or 2nd order IIR filter with Butterworth approximation. The optimal filter order and the cut-off frequency can be selected according to the proposed optimization procedure based on the autocorrelation function weighting.

Other tested methods were proven to be unsuitable for bleaching correction. The pixel-wise inverse mono-exponential fitting correction is not applicable in practice because of its extreme computational complexity. The high-pass FIR filtering is overall less effective and more complex than the IIR high-pass filtering, and cannot be recommended. The approach based on bank of filters provided lower image quality and increased computational demands, which makes it as well inappropriate.

By correcting the photobleaching effect, I was able to compute the 3rd and 4th order SOFI images with overall better image quality. The maximum computable SOFI order however depends on the SNR of the sample which decreases over time and limits the amount of data that can be used for SOFI reconstruction. Higher orders generally require higher SNR.

Future research can further focus on the preprocessing of the sample data. This may for example include more advanced denoising algorithms. Moreover the proposed methods should be tested on a larger database of samples. Special attention might be devoted to image sequences with temporally varying illumination. The proposed algorithms for bleaching correction could be further extended to 3D SOFI images.

9 References

[1]   J. Plášek, "SuperResolution in optical microscopy," 2015. [Online]. Available: http://www.cs.cas.cz/hanka/pmfa/1_15/plasek.pdf.

[2]   S. Stallinga and B. Rieger, "Accuracy of the Gaussian Point Spread Function model in 2D localization microscopy," *Optical Society of America,* vol. 18, no. 24, pp. 24461-24476, 2010.

[3]   K. R. Spring and M. W. Davidson, "Modulation Transfer Function," Nikon, 2015. [Online]. Available: http://www.microscopyu.com/articles/optics/mtfintro.html.

[4]   P. Kuttner, "An Instrument for Determining the Transfer Function of Optical Systems," *Applied Optics,* vol. 7, no. 6, pp. 1029-1033, 1968.

[5]   M. G. Gustafsson and J. R. Allen, "Structured Illumination Microscopy," Carl Zeiss, 2016. [Online]. Available: http://zeiss-campus.magnet.fsu.edu/articles/superresolution/supersim.html.

[6]   M. G. Gustafsson, "Surpassing the lateral resolution limit by a factor of two using structured illumination microscopy," *Journal of Microscopy,* no. 198, pp. 82-87, 2000.

[7]   R. H. a. C. Cremer, "Laterally Modulated Excitation Microscopy: Improvement of resolution by using a diffraction grating," *Proceedings of SPIE,* vol. 3568, pp. 185-196, 2000.

[8]   M. G. Gustafsson, L. Shao, P. M. Carlton, R. Wang, I. N. Gulubovskaya, Z. W. Cande, D. A. Agard and J. W. Sedat, "Three-dimensional resolution doubling in widefield fluorescence microscopy by structured illumination," *Biophysical journal,* vol. 94, no. 12, p. 4957–4970, 2008.

[9]   F. Orieux, E. Sepulveda, V. Loirette, B. Dubertret and J.-C. O. Marin, "Bayesian estimation for optimized structured illumination microscopy," *IEEE Transactions on Image Processing,* vol. 21, no. 2, pp. 601-614, 2012.

[10]   T. Lukeš, P. Křížek, Z. Švindrych, J. Benda, M. Ovesný, K. Fliegel, M. Klíma and G. M. Hagen, "Three-dimensional super-resolution structured illumination microscopy with maximum a posteriori probability image estimation," *Optics Express,* vol. 22, no. 24, p. 29805, Nov. 2014.

[11]   R. Heintzmann, "Structured illumination methods," in *Handbook of Biological Confocal Microscopy, 3rd ed., J. B. Pawley, Ed.*, New York, Springer, 2006, pp. 265-279.

[12]   A. Jost and R. Heintzmann, "Superresolution multidimensional imaging with structured illumination microscopy," *Annual Review of Materials Research,* vol. 43, no. 1, pp. 261-282, Jul. 2013.

[13]   T. Lukeš, G. M. Hagen, P. Křížek, Z. Švindrych, K. Fliegel and M. Klíma, "Comparison of image reconstruction methods for structured illumination microscopy," *Proceedings of SPIE - Biophotonics: Photonic Solutions for Better Health Care IV,* vol. 9129, pp. 1-13, May 8,2014.

[14]   S. Hell, "Far-field optical nanoscopy," *Science 316,* pp. 1153-1158, 2007.

[15]   Leica-Microsystems, "Leica TCS STED CW Brochure," 2011. [Online]. Available: https://www.leica-microsystems.com/fileadmin/downloads/Leica%20TCS%20STED%20CW/Brochures/Leica%20TCS%20STED%20CW-Brochure_EN.pdf.

[16]   M. Lauterbach, "STED Mikroskop PSFs," March 2010. [Online]. Available: https://commons.wikimedia.org/wiki/File:STED_Mikroskop_PSFs.jpg.

[17]   M. J. Rust, M. Bates and X. Zhuang, "Sub diffraction-limit imaging by stochastic optical reconstruction microscopy (STORM)," *Nature Methods,* vol. 3, no. 20, p. 793–796, Oct. 2006.

[18]   A. Lee, C. Bustamante, J. Y. Shin and S. H. Lee, "Counting single photoactivatable fluorescent molecules by photoactivated localization microscopy (PALM)," *Proceedings of the National Academy of Sciences,* vol. 109, no. 43, p. 17436–17441, 2012.

[19]   S. T. Hess, T. P. Girirajan and M. D. Mason, "Ultra-high resolution imaging by Fluorescence Photoactivation Localization Microscopy," *Biophysical Journal,* vol. 91, no. 11, p. 4258–4272, 2006.

[20]   W. M. Bates, B. Huang, G. T. Dempsey and X. Zhuang, "Multicolor Super-resolution Imaging with Photo-switchable," *Science,* vol. 317, pp. 1749-1753, Sep. 2007.

[21]   M. Heilemann, "Microscopic and spectroscopic methods," 2016. [Online]. Available: https://www.uni-frankfurt.de/49962827/Methods_Equipment..

[22]   T. Dertinger, R. Colyer, G. Lyer, S. Weiss and J. Enderlein, "Fast, background-free, 3D super-resolution optical fluctuation imaging (SOFI)," *Proceedings of the National Academy of Sciences of the United States of America,* vol. 106, no. 52, 29.Dec.2009.

[23]   S. Geissbuehler, A. Sharipov, A. Godinat, N. L. Bocchio, P. A. Sandoz, A. Huss, N. A. Jensen, S. Jakobs, J. Enderlein, F. G. v. d. Goot, E. A. Dubikovskaya, T. Lasser and M. Leutenegger, "Live-cell multiplane three-dimensional super-resolution optical fluctuation imaging," *NATURE COMMUNICATIONS,* vol. 5, no. 5830, pp. 1-7, Aug. 2014.

[24]   B. Hagen and E. L. Dereniak, "Gaussian profile estimation in two dimensions," *APPLIED OPTICS,* vol. 47, no. 36, pp. 6842-6848, Dec 2008.

[25]   D. B. Murphy and M. W. Davidson, Fundamentals of Light Microscopy and electronic Imaging 2nd. Edition, Wiley-Blackwell, 2013.

[26]   "Photobleaching in Fluorescence Imaging," Thermofisher, 2015. [Online]. Available: https://www.thermofisher.com/cz/en/home/life-science/cell-analysis/cell-analysis-learning-center/molecular-probes-school-of-fluorescence/protocols-troubleshooting/troubleshooting/photobleaching.html.

[27]   N. B. Vicente, J. E. D. Zamboni, J. F. Adur, E. V. Paravani and V. H. Casco, "Photobleaching correction in fluorescence microscopy images," *IOP Science,* 2007.

[28]   C. Rorabaugh, Digital Filter Designer's Handbook, New York: R.R. Donneley & Sons, 1993.

[29]   V. Davídek, M. Laipert and M. Vlček, Analog and Digital Filters, Praha: CVUT, 2000.

[30]   P. S. Jan Uhlíř, Digital Signal Processing, Praha: CVUT, 2002.

[31]   Z. Hrdina and F. Vejražka, "Discrete Fourier Transform," in *Signals and Systems*, Praha, CVUT, 2000, pp. 98-108.

[32]   R. M. Mersereau and M. J. Smith, Digital Filtering, New York: John Wiley & Sons, 1994.

[33]   "Minimum 4-term Blackman-Harris window," MathWorks, 2016. [Online]. Available: http://www.mathworks.com/help/signal/ref/blackmanharris.html.

[34]   "Blackman window," MathWorks, 2016. [Online]. Available: http://www.mathworks.com/help/signal/ref/blackman.html.

[35]   "Hamming window," MathWorks, 2016. [Online]. Available: http://www.mathworks.com/help/signal/ref/hamming.html.

[36]   "Nuttall-defined minimum 4-term Blackman-Harris window," MathWorks, 2016. [Online]. Available: http://www.mathworks.com/help/signal/ref/nuttallwin.html.

[37]   "Hann (Hanning) window," MathWorks, 2016. [Online]. Available: http://www.mathworks.com/help/signal/ref/hann.html.

[38]   Y.-P. Lin and P. Vaidyanathan, "Kaiser window," *IEEE SIGNAL PROCESSING LETTERS,* vol. 5, no. 6, pp. 132-134, 1998.

[39]   "Gaussian window," MathWorks, 2016. [Online]. Available: http://www.mathworks.com/help/signal/ref/gausswin.html?searchHighlight=gausswin.

[40]   "Flat top weighted window," MathWorks, 2016. [Online]. Available: http://www.mathworks.com/help/signal/ref/flattopwin.html.

[41]   A. Greensted, "FIR Filters by Windowing," 4 5 2010. [Online]. Available: http://www.labbookpages.co.uk/audio/firWindowing.html.

[42]   S. W. Smith, The Scientist and Engineer's Guide to Digital Signal Processing, California Technical Publishing, 2011.

[43]   M. Geissbuehler and T. Lasser, "Colormaps compatible with red-green color perception deficiencies," *Optical Express,* vol. 21, pp. 9862-9874, 2013.

[44]   M. Leutenegger, "Balanced super-resolution optical fluctuation imaging," 2014. [Online]. Available: https://documents.epfl.ch/users/l/le/leuteneg/www/BalancedSOFI/index.html.

[45]   T. Brakemann, A. C. Stiel, G. Weber, M. Andressen, I. Testa, T. Grotjohann, M. Leutenegger, U. Plessmann, H. Urlaub, C. Eggeling, M. C. Wahl, S. W. Hell and S. Jakobs, "A reversibly photoswitchable GFP-like protein with fluorescence excitation decoupled from switching.," *Nature Biotechnology,* vol. 29, no. 10, pp. 942-947, Sep. 2011.

[46]   W. Wallace, L. H. Scheafer and J. R. Swedlow, "Digital Image Processing - Artifacts and Aberrations in Deconvolution Analysis," Olympus, 2012. [Online]. Available: http://www.olympusmicro.com/primer/digitalimaging/deconvolution/deconartifacts.html.

[47]   M. Kaur and S. P. Kaur, "FIR Low Pass Filter Designing Using Different Window Functions and their Comparison using matlab," *International Journal of Advanced Research in Electrical Electronics and Instrumentation Engineering,* vol. 5, no. 2, pp. 753-758, Feb 2006.

[48]   S. Golestan, M. Ramezani, J. M. Guerrero, F. D. Freijedo and M. Monfared, "Moving Average Filter Based Phase-Locked Loops:Performance Analysis and Design Guidelines," *IEEE TRANSACTIONS ON POWER ELECTRONICS,* vol. 29, no. 6, pp. 2750-2763, June 2014.

[49]   M. d. F. Juan, "The DC Blocking Filter," 29 1 2007. [Online]. Available: http://www.mathworks.com/matlabcentral/fileexchange/13792-the-dc-blocking-filter.

[50]   "Filter Banks - Matlab & Simulink," Mathworks, 2016. [Online]. Available: http://www.mathworks.com/help/dsp/ug/filter-banks.html?refresh=true.

[51]   A. Mertins, Signal Analysis: Wavelets, Filter Banks, Time-Frequency Transforms and Applications, John Wiley & Sons Ltd, 1999.

[52]   S. S. Kanchan Lata Kashyap, "Noise Removal of Facial Expression Images using Wiener Filter," in *National Conference on Emerging Trends in Computer Science and Information Technology (ETCSIT)*, 2011.

[53]   H. Chen and S. Chen, A Moving Average based Filtering System with its Application to Real-time QRS, Department of Electronic Engineering, Chang Gung University, Taiwan, 2003.

[54]   H. Deschout, T. Lukes, A. Sharipov, D. Szlag, L. Feletti, W. Vandenberg, P. Dedecker, J. Hofkens, M. Leutenegger, T. Lasser and A. Radenovic, "Complementarity of PALM and SOFI for super-resolution live cell imaging of focal adhesions," *Biological Physics,* pp. 1-24, Apr. 2016.
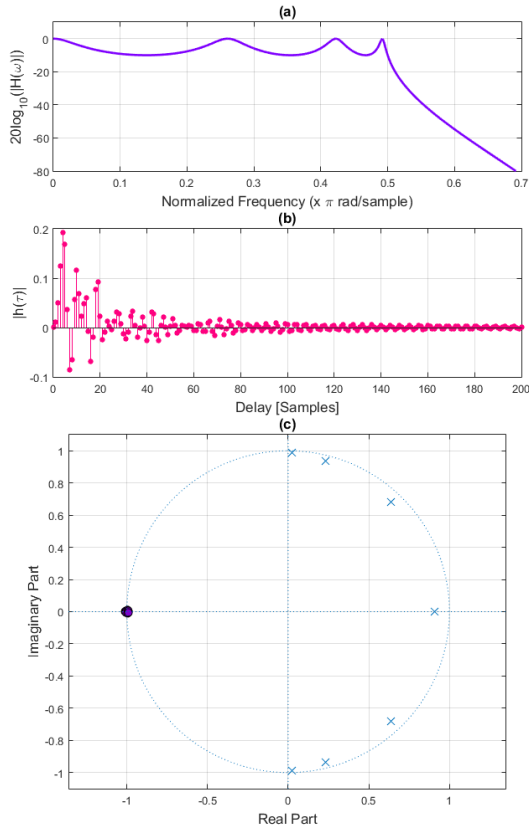
Figure 52 Chebyshev low-pass 7th order filter with $\omega_c = 0.5$ π rad/sample and passband ripple of 3dB. Its transfer function (a), Impulse response (b) and Zplane (c) - poles (cross), zeros (point).
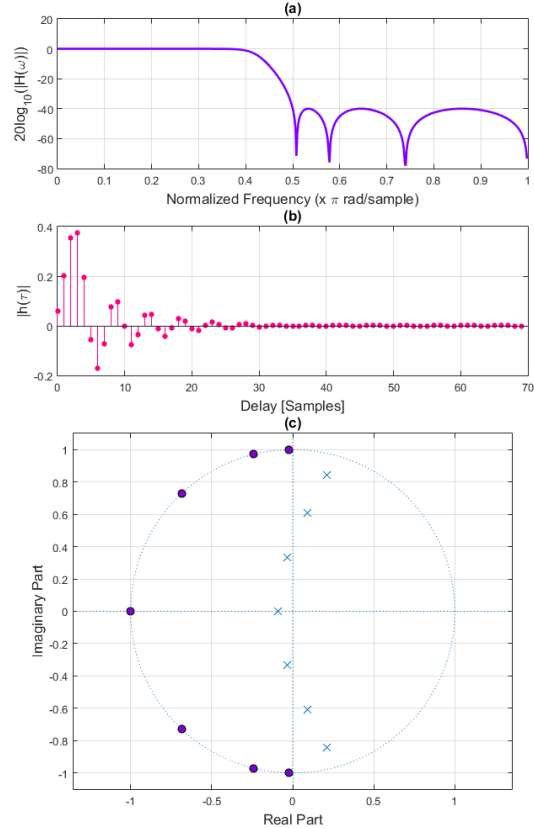
Figure 53 Inverse Chebyshev digital low-pass 7th order filter with $\omega_c = 0.5$ π rad/sample and stopband ripple of 40dB. Its transfer function (a), Impulse Response (b) and the Zplane (c) - poles (cross) and zeros (point).
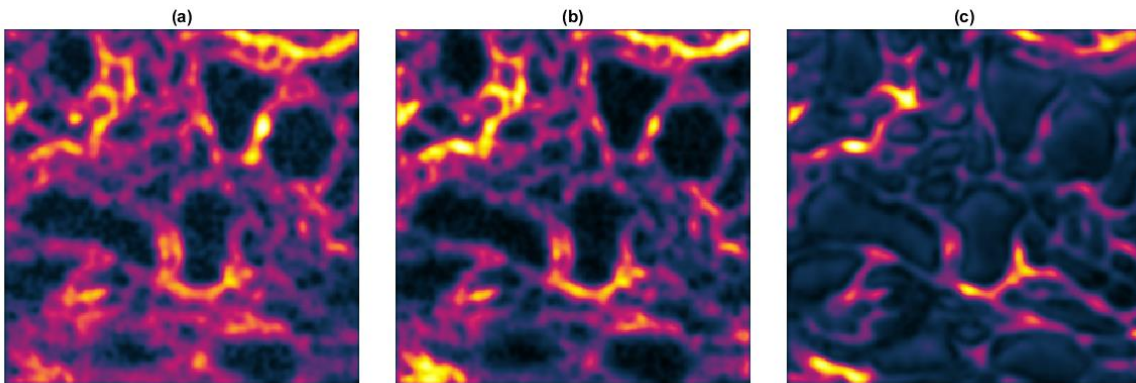

Figure 54 Sample 1. 3rd order SOFI Images Colored with morgenstemning colormap [43]. Original image size 100x100 pixels, 3000 frames, field of view 9.24 μm. SOFI image (a) with pixel-wise inverse mono-exponential fitting correction – computing time 105 minutes on Intel core i5-750 processor, (b) with the bleaching correction using the moving average subtraction technique, 260th order, (c) with frame-wise inverse mono-exponential fitting correction.
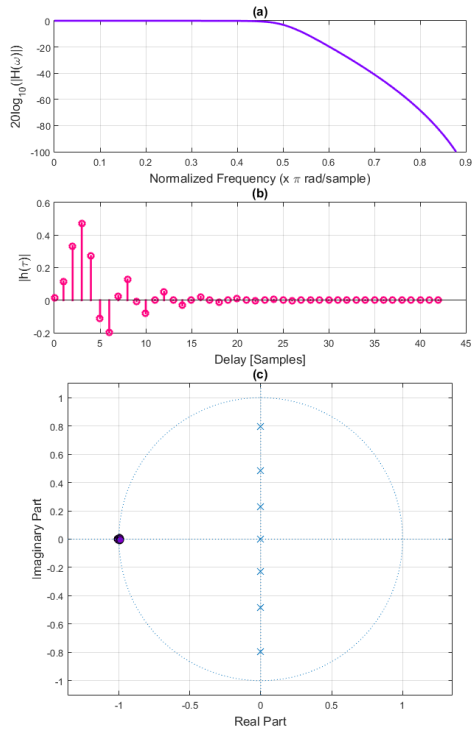
Figure 55 Butterworth digital low-pass 7th order filter with ω_c = 0.5 π rad/sample. Its transfer function (a), impulse response (b) and the Zplane (c) - poles (Cross) and zeros (Point).

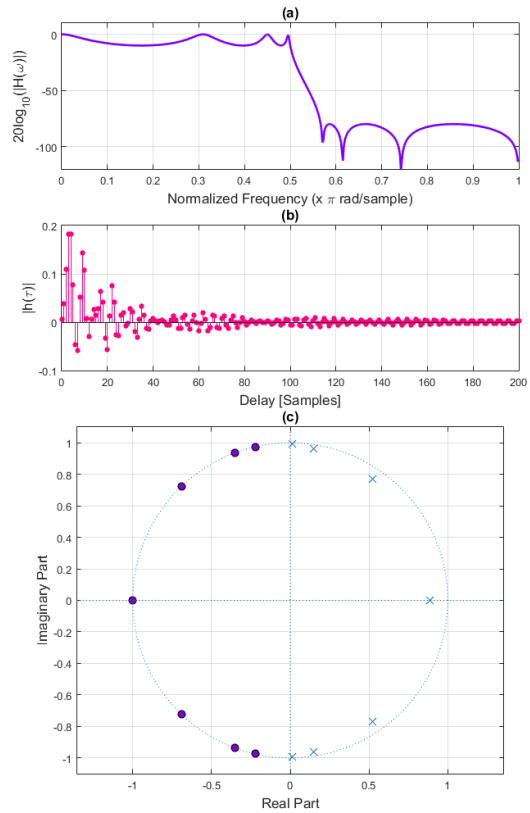**Figure 56 Cauer digital low-pass 7th order filter with ω_c = 0.5 π rad/sample, passband ripple of 10dB and stopband ripple of 80dB. Its transfer function (a), impulse response (b) and the Zplane (c) - poles (Cross) and zeros (Point).**
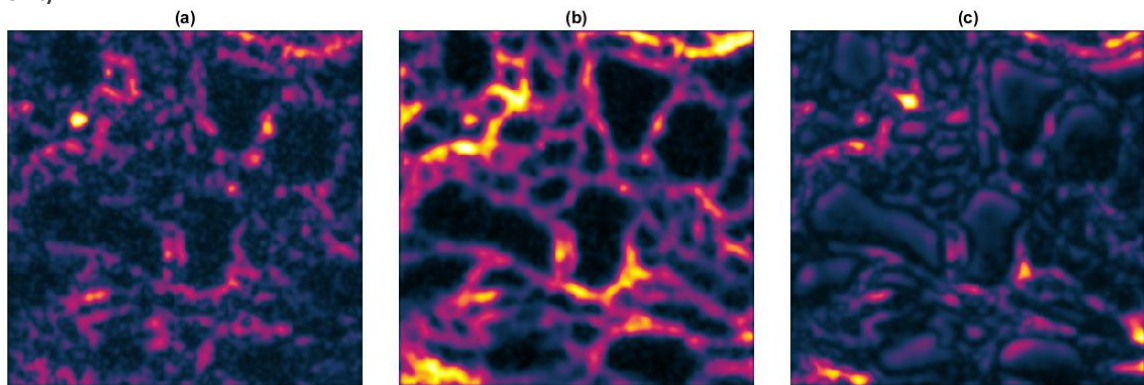

Figure 57 Sample1. 4th order SOFI Images with morgenstemning colormap [43]. Original image size 100x100 pixels, 3000 frames, field of view 9.24 µm. SOFI image (a) with pixel-wise inverse mono-exponential fitting correction – computing time 105 minutes on Intel core i5-750 processor, (b) – with the bleaching correction using the moving average subtraction technique, 260th order, (c) with frame-wise inverse mono-exponential fitting correction.
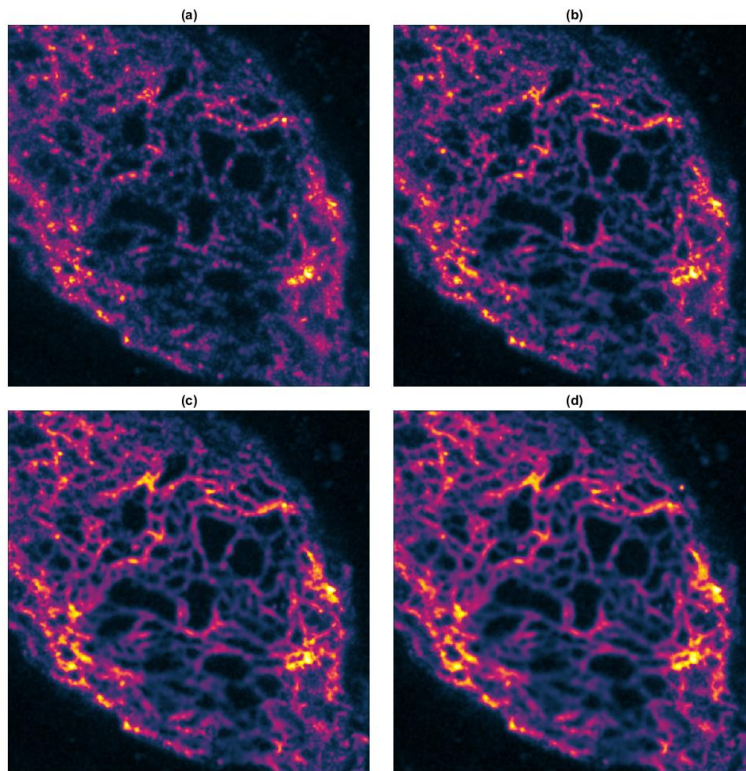
Figure 58 Sample 1. 4th order SOFI Images with morgenstemning colormap [43]. Original image size 200x200 pixels, field of view 18.84 μm. All processed by moving average subtraction technique, 300th order. SOFI image (a) reconstructed from 1000 frames, (b) from 2000 frames, (c) from 3000 frames and (d) from 4000 frames.
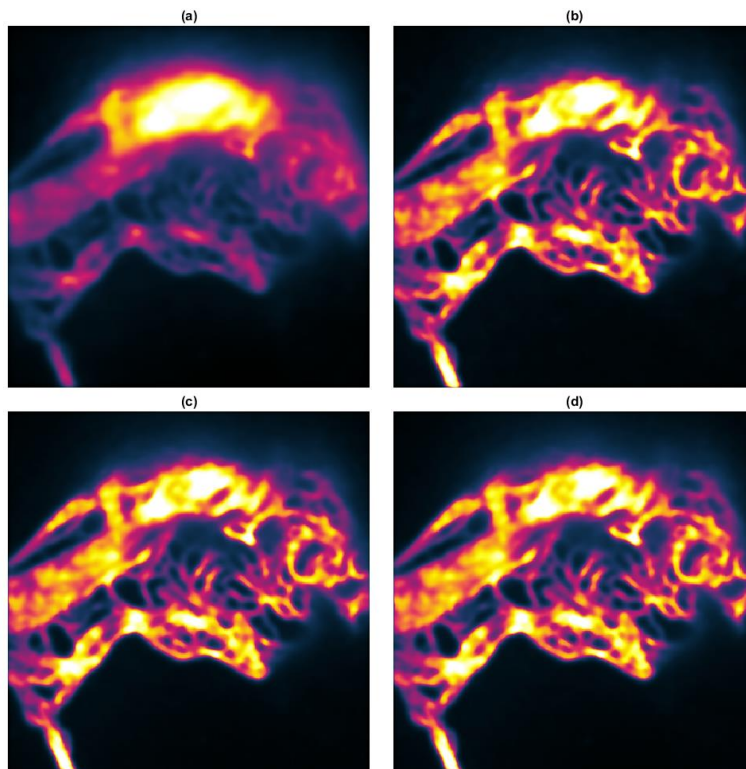

Figure 59 Sample 2. 2nd order SOFI Images with morgenstemning colormap [43]. Original image size 200x200 pixels, 2000 frames, field of view 18.84 μm. SOFI image (a) without bleaching correction, (b) with inverse mono-exponential fitting correction, (c) with inverse mono-exponential fitting and division into subsequences correction, (d) with the bleaching correction using the moving average subtraction technique, 300th order.

11Appendix B: Content of the attached DVD

- TersVojtech_DP_BleachingCorrection.pdf
- TersVojtech_DP_BleachingCorrection.docx

Samples

- `GreenND02_405ND01_365ND11_DU897_BV_1544.tif`
- `GreenND02_405ND05_365ND09_DU897_BV_1561.tif`

Matlab functions

- DIPAllFilter.m
- DIPAVGSweep.m
- DIPBankDecompositionASym.m
- DIPBankDecompositionSym.m
- DIPCalculation.m
- DIPCustomImageLoad.m
- DIPFilterConstruction.m
- DIPFIRSweep.m
- DIPIIRSweep.m
- DIPInvWiener.m
- DIPMain.m
- DIPSOFIBankFilter.m
- DIPSOFICumulants.m
- DIPSOFICumulantsFramed.m
- DIPSweepFirWindTypes.m
- morgenstemning.m

Dir SampleModels

- BankFilters.m
- ButterWorth.m
- ButterWorthSyms.m
- Cauer.m
- Causality.m
- Chebyshev.m
- ExpMultiSingleFit.m
- FilterTypes.m
- FIRHammingNuttall.m
- FirstOrderIIR.m
- FIRvsIIR.m
- GaussianPowers.m
- InverseChebyshev.m
- MovingAverage.m
- OptimumSelection.m
- PSFDemo.m
- SampleFuntion.m
- Superposition.m
- SOFIFrameIncrease.m

Dir VisioFiles

- 2NFilterBank.vsdx
- 2NFilterBankAsym.vsdx
- BasicSystem.vsdx
- DCBlockingFilter.vsdx
- Jablonski.vsdx
- SimpleFIR.vsdx
- SOFITimeCapture.vsdx

Dir Data

- **Dir utils**
  - load_tifFile.m
  - saveImageStack.m
  - statusbar.m
- **Dir SOFI**
  - runDecCurve.m
  - sofiBalance.m
  - sofiCumulants2D.m
  - sofiCumulants2Dt.m
  - sofiFlatten.m
  - sofiGrids.m
  - sofiGridsT.m
  - sofiLinearize.m
  - sofiPSFfwhm.m
  - Dir private

Recommended testing settings are included in the DIPMain.m script. Additional info can be found in Readme.txt